

Wall cooling effect on spectra and structures of thermodynamic variables in hypersonic turbulent boundary layers

Dehao Xu¹, Jianchun Wang^{2,†} and Shiyi Chen^{3,2,1‡}

¹State Key Laboratory of Turbulence and Complex Systems, College of Engineering, Peking University, Beijing 100871, People's Republic of China

²Department of Mechanics and Aerospace Engineering, Southern University of Science and Technology, Shenzhen 518055, People's Republic of China

³Eastern Institute for Advanced Study, Ningbo 315200, People's Republic of China

(Received xx; revised xx; accepted xx)

The wall cooling effect on the spectra and structures of thermodynamic variables are investigated in hypersonic turbulent boundary layers. The density and temperature can be divided into the acoustic and entropic modes based on the Kovasznay decomposition. The intensities of the pressure and the acoustic modes of density and temperature attain the maximum values near the wall, while those of the entropy and the entropic modes of density and temperature achieve their primary peaks near the edge of boundary layer. In the near-wall region, the pressure and the acoustic modes of density and temperature are significantly enhanced when the wall is strongly cooled, which can be attributed to the appearance of the travelling-wave-like alternating positive and negative structures. Moreover, the intensities of the entropy and the entropic modes of density and temperature become stronger near the wall as the wall temperature decreases, due to the appearance of the streaky entropic structures. The streaky entropic structures are mainly caused by the advection effect of the strong positive wall-normal gradient of the mean temperature associated with ejection and sweep events. It is also found that the profiles of the intensities of the entropy, density and temperature are similar to each other far from the wall, which are mainly due to the reason that the entropic modes are dominant in the fluctuating density and temperature in the far-wall region. The acoustic modes of density and temperature only have significant contributions in the near-wall region.

Key words:

1. Introduction

The mechanisms of the hypersonic turbulent boundary layers are of great importance in aerospace industry due to the direct application to the hypersonic vehicles (Smits & Dussauge 2006; Gatski & Bonnet 2009). It has been widely observed that the cold wall can significantly enhance the compressibility effect near the wall in hypersonic turbulent boundary layers (Duan *et al.* 2010; Zhang *et al.* 2017, 2018; Xu *et al.* 2021a,b,

† Email address for correspondence: wangjc@sustech.edu.cn

‡ Email address for correspondence: chensy@sustech.edu.cn

2022b,c,a; Huang *et al.* 2022). Therefore, the systematic investigations of the properties of the physical quantities in the cooled wall hypersonic turbulent boundary layers are extraordinarily critical to better understanding of the underlying mechanisms and more accurate physics-based modelling for this type of flows.

Most of the previous investigations about the hypersonic turbulent boundary layers were concentrated on the flow statistics of velocities (Duan *et al.* 2010, 2011; Lagha *et al.* 2011; Chu *et al.* 2013a; Zhang *et al.* 2018; Xu *et al.* 2021a,b, 2022b,c,a; Huang *et al.* 2022). Duan *et al.* (2010) performed direct numerical simulation (DNS) of hypersonic turbulent boundary layers at Mach number 5 with isothermal boundary condition. The ratio of the wall-to-edge temperature is ranging from 1.0 to 5.4. The effect of wall cooling on Morkovin's scaling, Walz's equation, the strong Reynolds analogy (SRA), turbulent kinetic energy budgets, compressibility effect and near-wall coherent structures were systematically investigated. They found that many scaling relations for the non-adiabatic hypersonic turbulent boundary layers are similar to those found in adiabatic wall cases, and the compressibility effect is insignificantly enhanced by wall cooling. Furthermore, Zhang *et al.* (2018) developed DNS databases of spatially evolving zero-pressure-gradient compressible turbulent boundary layers with nominal free-stream Mach number ranging from 2.5 to 14 and wall-to-recovery temperature ranging from 0.18 to 1.0. They assessed the performance of compressibility transformations, including the Morkovin's scaling and SRA, as well as the mean velocity and temperature scaling. Recently, a series of researches were aiming to reveal the effect of wall cooling on other complicated flow statistics beyond the well-observed compressibility transformations and the mean velocity and temperature scaling (Xu *et al.* 2021a,b, 2022b,c,a). Xu *et al.* (2021a,b) performed the DNS of hypersonic turbulent boundary layers at Mach numbers 6 and 8 with wall-to-recovery temperature ranging from 0.15 to 0.8. They used the Helmholtz decomposition to divide the fluctuating velocities into the solenoidal and dilatational components. They investigated the interactions among mean and fluctuating fields of kinetic and internal energy (Xu *et al.* 2021a) as well as the kinetic energy transfer across different scales (Xu *et al.* 2021b). Furthermore, the flow topology and its effect on the kinetic energy transfer across different scales were also systematically investigated in Xu *et al.* (2022b,c). In order to explain the possible reasons of the overshoot phenomena of the wall skin friction and wall heat transfer in transitional hypersonic boundary layers, Xu *et al.* (2022a) applied the decomposition method on the wall skin friction and heat transfer coefficients based on the two-fold repeated integration. Moreover, the effect of the wall cooling on the wall skin friction and heat transfer decomposition in hypersonic turbulent boundary layers was also discussed.

However, most of the previous studies were focused on the flow statistics and structures of velocities, while the mechanisms of the thermodynamic statistics in hypersonic turbulent boundary layers were less studied (Duan *et al.* 2016; Zhang *et al.* 2017; Ritos *et al.* 2019; Zhang *et al.* 2022; Cogo *et al.* 2022). Recently, Zhang *et al.* (2022) investigated the wall cooling effect on pressure fluctuations in compressible turbulent boundary layers. They explored the generating mechanisms of pressure fluctuations by dividing the pressure fluctuations into five components, among which the rapid pressure, slow pressure and compressible pressure are dominant. Furthermore, Cogo *et al.* (2022) investigated the high-Reynolds-number effect in hypersonic turbulent boundary layers. They studied the structural properties of the uniform streamwise momentum and uniform temperature regions in the high-speed regime. Furthermore, they also evaluated the accuracy of different compressibility transformations and temperature-velocity relations at moderate-high Reynolds numbers. A revised scaling for the characteristic length scales of the spanwise spectra of the fluctuating velocity and temperature at various wall

distances was proposed based on the local mean shear. Nevertheless, the wall cooling effect on the multi-scale properties and the spatial structures of the pressure, density, temperature and entropy in hypersonic turbulent boundary layers need more systematic investigations, for the sake of a better understanding of the underlying mechanisms and more accurate physics-based modelling of the thermodynamic variables.

The goal of this study is to systematically explore the wall cooling effect on the spectra and structures of the thermodynamic variables in hypersonic turbulent boundary layers by direct numerical simulation. The fluctuating density and temperature are divided into the acoustic and entropic modes based on the Kovaszny decomposition (Kovaszny 1953; Chassaing *et al.* 2002; Gauthier 2017; Wang *et al.* 2019). The streamwise and spanwise spectra of the thermodynamic variables are systematically studied to figure out the multi-scale properties and spatial structures of thermodynamic variables. The streamwise and spanwise spectra of the fluctuating streamwise velocity are also investigated aiming for comparing with those of the thermodynamic variables. It is found that the wall cooling effect on the spectra and structures of the thermodynamic variables are much larger than those of the fluctuating streamwise velocity.

The remainder of the paper is organized as follows. The governing equations and simulation parameters are outlined in Section 2. The turbulent intensities of the streamwise velocity and thermodynamic variables are shown in Section 3. Section 4 presented the streamwise and spanwise spectra of the streamwise velocity and thermodynamic variables. Some discussions are given in Section 5. Finally, summary and conclusions are given in Section 6.

2. Governing equations and simulation parameters

The compressible Navier-Stokes equations can be non-dimensionalised by a set of reference scales: the reference length L_∞ , free-stream density ρ_∞ , velocity U_∞ , temperature T_∞ , pressure $p_\infty = \rho_\infty U_\infty^2$, energy per unit volume $\rho_\infty U_\infty^2$, viscosity μ_∞ and thermal conductivity κ_∞ . Therefore, there are three non-dimensional governing parameters, namely the Reynolds number $Re = \rho_\infty U_\infty L_\infty / \mu_\infty$, Mach number $M = U_\infty / c_\infty$ and Prandtl number $Pr = \mu_\infty C_p / \kappa_\infty$. The ratio of specific heat at constant pressure C_p to that at constant volume C_v is defined as $\gamma = C_p / C_v = 1.4$. The parameter α is defined as $\alpha = Pr Re (\gamma - 1) M^2$, where $Pr = 0.7$.

The following compressible dimensionless Navier-Stokes equations in the conservative form are solved numerically (Liang & Li 2015; Xu *et al.* 2021a,b, 2022b,c,a)

$$\frac{\partial \rho}{\partial t} + \frac{\partial (\rho u_j)}{\partial x_j} = 0, \quad (2.1)$$

$$\frac{\partial (\rho u_i)}{\partial t} + \frac{\partial [\rho u_i u_j + p \delta_{ij}]}{\partial x_j} = \frac{1}{Re} \frac{\partial \sigma_{ij}}{\partial x_j}, \quad (2.2)$$

$$\frac{\partial E}{\partial t} + \frac{\partial [(E + p) u_j]}{\partial x_j} = \frac{1}{\alpha} \frac{\partial}{\partial x_j} \left(\kappa \frac{\partial T}{\partial x_j} \right) + \frac{1}{Re} \frac{\partial (\sigma_{ij} u_i)}{\partial x_j}, \quad (2.3)$$

$$p = \rho T / (\gamma M^2), \quad (2.4)$$

where ρ , u_i , T and p are the density, velocity component, temperature and pressure, respectively. The viscous stress σ_{ij} is defined as

$$\sigma_{ij} = \mu \left(\frac{\partial u_i}{\partial x_j} + \frac{\partial u_j}{\partial x_i} \right) - \frac{2}{3} \mu \theta \delta_{ij}, \quad (2.5)$$

where $\theta = \partial u_k / \partial x_k$ is the velocity divergence, and the viscosity μ is determined by the Sutherland's law. The total energy per unit volume E is

$$E = \frac{p}{\gamma - 1} + \frac{1}{2} \rho (u_j u_j). \quad (2.6)$$

The convection terms of the compressible governing equations are discretized by a hybrid scheme. In order to judge on the local smoothness of the numerical solution, the modified Jameson sensor (Jameson *et al.* 1981) is used in the hybrid scheme, which can be given by (Dang *et al.* 2022)

$$\begin{aligned} \phi_i &= \frac{|-p_{i-1} + 2p_i - p_{i+1}|}{p_{i-1} + 2p_i + p_{i+1}}, \\ \phi_j &= \frac{|-p_{j-1} + 2p_j - p_{j+1}|}{p_{j-1} + 2p_j + p_{j+1}}, \\ \phi_k &= \frac{|-p_{k-1} + 2p_k - p_{k+1}|}{p_{k-1} + 2p_k + p_{k+1}}, \end{aligned} \quad (2.7)$$

$$\Theta = \phi_i + \phi_j + \phi_k. \quad (2.8)$$

The threshold Θ_1 is set to 0.02 (Dang *et al.* 2022). When $\Theta \leq \Theta_1$, the eighth-order central difference scheme is used; when $\Theta > \Theta_1$, the seventh-order weighted essentially non-oscillatory scheme (Balsara & Shu 2000) is applied. Furthermore, the viscous terms are approximated by an eighth-order central difference scheme. A third-order total variation diminishing type of Runge-Kutta method is utilized for time advancing (Shu & Osher 1988). The compressible governing equations are numerically solved by the OPENCFD code, which has been widely validated in compressible transitional and turbulent wall-bounded flows (Liang & Li 2015; Xu *et al.* 2021a,b, 2022b,c,a; Dang *et al.* 2022). The schematic of the hypersonic transitional and turbulent boundary layers is shown in figure 1. The spatially evolving hypersonic transitional and turbulent boundary layer is numerically simulated under the inflow and outflow boundary conditions, a wall boundary condition, an upper far-field boundary condition, and a periodic boundary condition in the spanwise direction. A time-independent laminar compressible boundary-layer similarity solution is applied at the inflow boundary. The laminar flow is disturbed by the wall blowing and suction region, and then transitioned to the fully developed turbulent state. Moreover, in order to inhibit the reflection of disturbance due to the numerical treatment of the outflow boundary condition, a progressively coarse grid is implemented in the streamwise direction near the outflow boundary condition. The non-slip and isothermal boundary conditions are applied for the wall boundary, and the non-reflecting boundary condition is imposed for the upper boundary. More detailed descriptions can refer to Pirozzoli *et al.* (2004); Liang & Li (2015); Xu *et al.* (2021a,b, 2022b,c,a).

In this study, \bar{f} denotes the Reynolds average (spanwise and time average) of flow field f , and the fluctuating component of the Reynolds average is $f' = f - \bar{f}$. Furthermore, $\overline{\rho f} = \bar{\rho} \bar{f}$ represents the Favre average of f , and the fluctuating component is $f'' = f - \overline{\rho f} / \bar{\rho}$.

The DNS of three hypersonic transitional and turbulent boundary layers at Mach number 8 with different wall temperatures are performed and the fundamental parameters of the database are listed in table 1. The free-stream temperature T_∞ is prescribed to be $T_\infty = 169.44K$. Temperature T_w is the wall temperature, and the recovery temperature T_r can be defined as $T_r = T_\infty (1 + r((\gamma - 1)/2) M_\infty^2)$ with recovery factor $r = 0.9$ (Duan *et al.* 2010; Xu *et al.* 2022a). The coordinates along the streamwise, wall-normal and spanwise directions are represented by x , y and z respectively. The computational

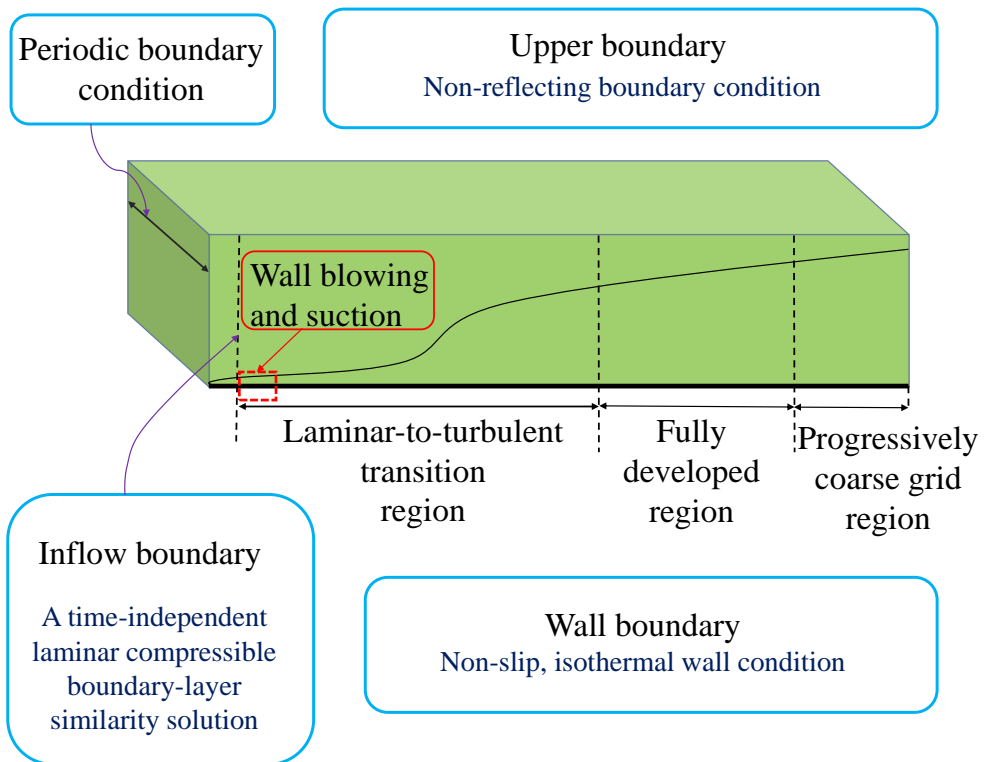


FIGURE 1. The schematic of the hypersonic transitional and turbulent boundary layers.

domains L_x , L_y and L_z are nondimensionalized by the inflow boundary layer thickness δ_{in} , and the symbols N_x , N_y and N_z represent the grid resolutions along the streamwise, wall-normal and spanwise directions respectively.

It should be pointed out that the no-ideal gas effect, as well as the non-equilibrium and radiative effects are neglected in the present DNS databases. The reasons are as follows. It is noted that the free-stream temperature T_∞ is prescribed to be $T_\infty = 169.44K$ in the present study. The largest temperature in the highest wall temperature case M8T08 is approximately 1700K. In the previous studies, the maximum temperatures of cases “M7”, “M8” and “M12” in [Duan et al. \(2011\)](#) and $M_\infty = 7.5, 10, 15$ and 20 in [Lagha et al. \(2011\)](#) are much larger than that of M8T08, and the no-ideal gas effect, as well as the non-equilibrium and radiative effects were also neglected in their study. Therefore, the neglect of the no-ideal gas, non-equilibrium and heat radiative effects is a reasonable simplification for the present study of the hypersonic turbulent boundary layers. The influence of the no-ideal gas, non-equilibrium and radiative effects in the hypersonic turbulent boundary layers will be considered in the future.

Three sets of data in a small streamwise window of $[x_a - 0.5\delta, x_a + 0.5\delta]$ extracted from the fully developed region of the above three transitional and hypersonic turbulent boundary layers are used for following statistical analysis, where x_a is the reference streamwise location selected for statistical analysis, and δ is the boundary layer thickness at the streamwise location x_a . It is noted that a similar technique has been used by the previous studies of [Pirozzoli & Bernardini \(2011\)](#), [Zhang et al. \(2018\)](#) and [Huang et al.](#)

Case	M	Re	T_w/T_∞	T_w/T_r	$L_x/\delta_{in} \times L_y/\delta_{in} \times L_z/\delta_{in}$	$N_x \times N_y \times N_z$
M8T015	8	5.2×10^4	1.9	0.15	$1000 \times 95 \times 42$	$6000 \times 500 \times 600$
M8T04	8	2.6×10^5	5.0	0.4	$1500 \times 97 \times 47$	$7000 \times 400 \times 500$
M8T08	8	8.0×10^5	10.03	0.8	$1700 \times 103 \times 51$	$7000 \times 400 \times 400$

TABLE 1. Summary of computational parameters for the three DNS database at Mach number 8 with different wall temperatures.

Case	x_a/δ_{in}	Δx^+	Δy_w^+	Δy_e^+	Δz^+	Re_τ	Re_τ^*	δ/δ_{in}
M8T015	870	8.3	0.50	6.4	4.1	920	1715	15.4
M8T04	1100	8.0	0.51	5.9	4.4	700	3885	14.3
M8T08	1580	8.4	0.50	6.1	5.2	700	7888	16.7

TABLE 2. The fundamental parameters of the three sets of data.

(2022), and the width of the streamwise window in this study is consistent with that of Huang *et al.* (2022). The fundamental parameters of the three sets of data are listed in table 2. The friction Reynolds number Re_τ is defined as $Re_\tau = \bar{\rho}_w u_\tau \delta / \bar{\mu}_w$, where $\bar{\rho}_w$ and $\bar{\mu}_w$ are the mean wall density and wall viscosity respectively, and $u_\tau = \sqrt{\tau_w / \bar{\rho}_w}$ and $\tau_w = (\mu \partial \bar{u} / \partial y)_{y=0}$ are the friction velocity and the wall shear stress respectively. Furthermore, $\Delta x^+ = \Delta x / \delta_\nu$, $\Delta y_w^+ = \Delta y_w / \delta_\nu$, $\Delta y_e^+ = \Delta y_e / \delta_\nu$ and $\Delta z^+ = \Delta z / \delta_\nu$ are the normalized spacing of the streamwise direction, the first point off the wall, the wall-normal grid at the edge of the boundary layer and the spanwise direction respectively, where $\delta_\nu = \bar{\mu}_w / (\bar{\rho}_w u_\tau)$ is the viscous length scale. The semi-local lengthscale is defined as $\delta_\nu^* = \bar{\mu} / (\bar{\rho} u_\tau^*)$, where $u_\tau^* = \sqrt{\tau_w / \bar{\rho}}$ (Huang *et al.* 1995). The semi-local Reynolds number can be defined as $Re_\tau^* = \delta / (\delta_\nu^*)_e$. It is noted that the grid resolutions Δx^+ , Δy_w^+ , Δy_e^+ and Δz^+ in three cases are comparable and even smaller than many previous investigations including Duan *et al.* (2010), Pirozzoli & Bernardini (2013), Zhang *et al.* (2018) and Huang *et al.* (2022), indicating that the grid resolutions of the present DNS study are fine enough. Furthermore, the accuracy of the DNS cases in this study are validated via comparisons with the available DNS database in Zhang *et al.* (2018) in Appendix A.

The mean density and temperature profiles along wall-normal direction are shown in figure 2. Here the ‘‘turning points’’ marked by the green circles represent the minimum values of the mean density in figure 2 (a), (b) and (c), and the maximum values of the mean temperature in figure 2 (d), (e) and (f). The wall unit scaling is defined as $y^+ = y / \delta_\nu$, and the semi-local scaling is defined as $y^* = y / \delta_\nu^*$. It is noted that the wall unit scaling y^+ and the semi-local scaling y^* are the inner scaling in order to reveal the scaling relation in the near-wall region, while the outer scaling y / δ shows the statistical behaviour in the far-wall region.

The mean density and temperature are significantly influenced by the wall temperature. When the wall temperature is close to the recovery temperature T_r (‘‘M8T08’’ case), the mean temperature is nearly constant near the wall, and then decreases drastically when $y^+ > 4$. However, in ‘‘M8T04’’ and ‘‘M8T015’’, the mean temperature initially increases near the wall. After reaching the maximum value at the turning point, the mean temperature then decreases as y increases. It is also found that as the wall

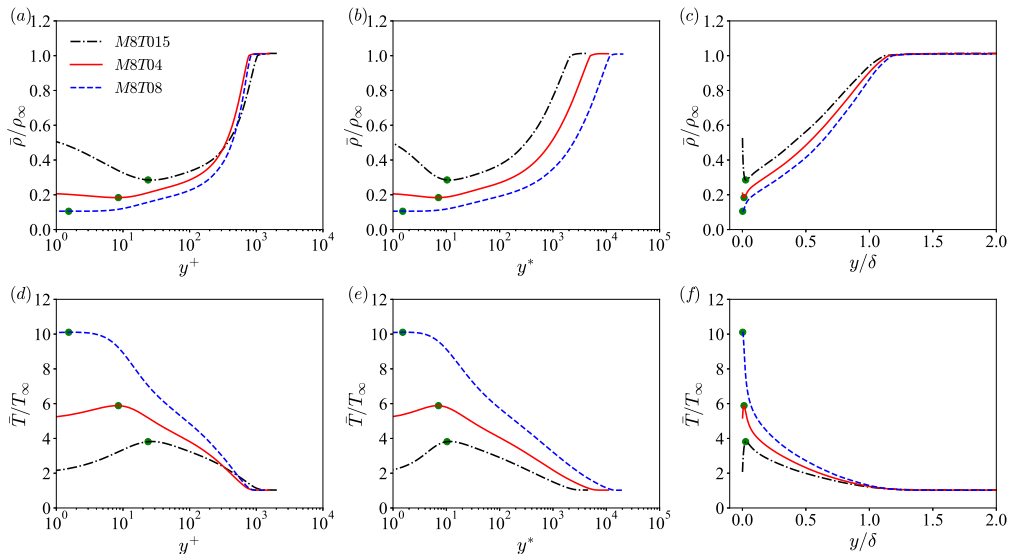


FIGURE 2. (a) (b) and (c): The mean density profile along wall-normal direction plotted against (a) wall unit scaling (y^+), (b) semi-local scaling (y^*) and (c) outer scaling (y/δ). (d) (e) and (f): The mean temperature profile along wall-normal direction plotted against (d) wall unit scaling (y^+), (e) semi-local scaling (y^*) and (f) outer scaling (y/δ). Here the “turning points” marked by the green circles represent the minimum values of the mean density in (a), (b) and (c), and the maximum values of the mean temperature in (d), (e) and (f).

temperature decreases, the positive values of the wall-normal gradient of the mean temperature become larger below the wall-normal location of the turning point, while the negative values of the wall-normal gradient of the mean temperature become smaller above it. Furthermore, when the wall temperature becomes cooler, the maximum value of the mean temperature decreases, while the wall-normal location y^+ of the turning point increases under the wall unit scaling. The semi-local scaling y^* can significantly decrease the discrepancy of the wall-normal locations of turning points in different wall temperature cases. It should be noted that the mean density profiles reveal the opposite variation trends compared with the mean temperature profiles.

In order to investigate the effect of wall temperature on the compressibility effect, the turbulent Mach number $M_t = \sqrt{u_i''u_i''}/\bar{c}$ and the root mean square (r.m.s) values of the local Mach number based on the fluctuating velocities M'_{rms} are evaluated in figure 3. Here the local Mach number based on the fluctuating velocities M' is defined as $M' = \sqrt{u_i''u_i''}/c$, and c represents the local sound speed. As the wall temperature decreases, the peak values of M_t and M'_{rms} increase, indicating that the cooling wall can enhance the compressibility effect, which is consistent with many previous studies including Zhang *et al.* (2018), Xu *et al.* (2021b) and Zhang *et al.* (2022). Moreover, it is shown in figure 3 (a) and (d) that the wall-normal locations y^+ of the peak values of M_t and M'_{rms} increase under the wall unit scaling as the wall temperature decreases, while it is found in figure 3 (b) and (e) that the M_t and M'_{rms} profiles against the semi-local scaling attain their peaks at almost the same values of y^* in different wall temperature cases.

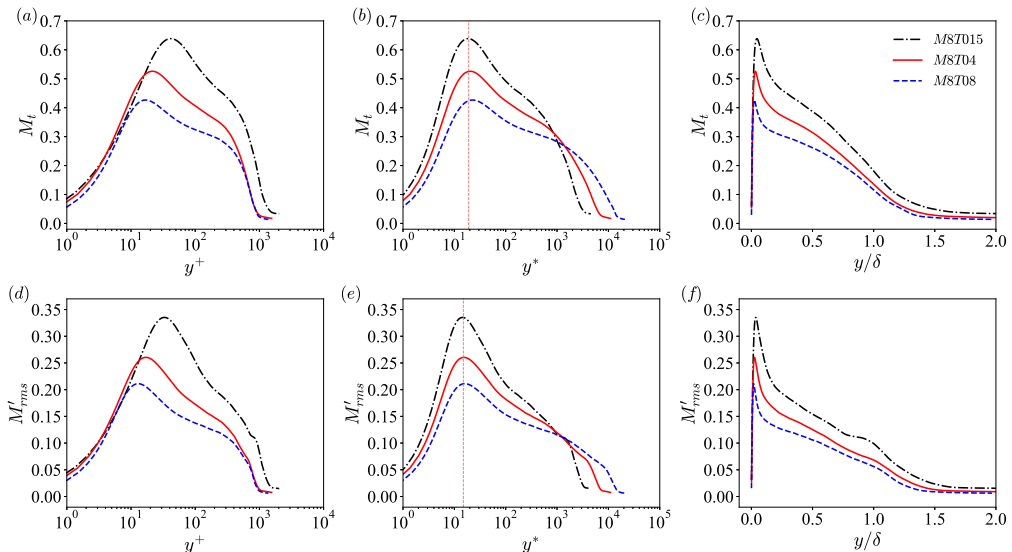


FIGURE 3. (a) (b) and (c): The turbulent Mach number M_t along wall-normal direction plotted against (a) wall unit scaling (y^+), (b) semi-local scaling (y^*) and (c) outer scaling (y/δ). The vertical dashed line represents $y^* = 19$ in (b). (d) (e) and (f): The r.m.s values of the local Mach number M'_{rms} along wall-normal direction plotted against (d) wall unit scaling (y^+), (e) semi-local scaling (y^*) and (f) outer scaling (y/δ). The vertical dashed line represents $y^* = 19$ in (e).

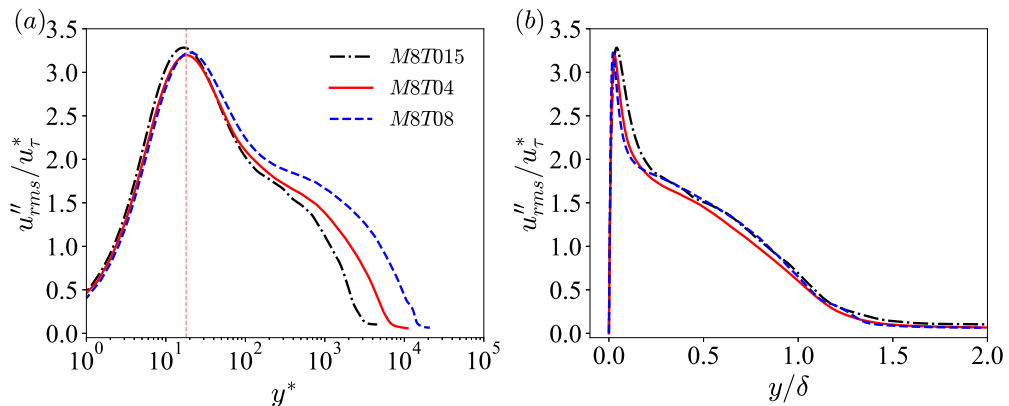


FIGURE 4. The normalised turbulent intensity of the streamwise velocity u''_{rms}/u^* plotted against (a) semi-local scaling (y^*) and (b) outer scaling (y/δ). The vertical dashed line represents $y^* = 18$ in (a).

3. The turbulent intensities of the streamwise velocity and the thermodynamic variables

The normalised turbulent intensity of the streamwise velocity u''_{rms}/u^* along wall-normal direction is shown in figure 4. It is found that u''_{rms}/u^* attains its peak in the buffer layer (approximately $y^* \approx 18$). Furthermore, the peak values of u''_{rms}/u^* are similar in “M8T04” and “M8T08” cases. However, the peak value is slightly larger in “M8T015”, which can be ascribed to the strongly colder wall temperature and slightly larger friction Reynolds number Re_τ .

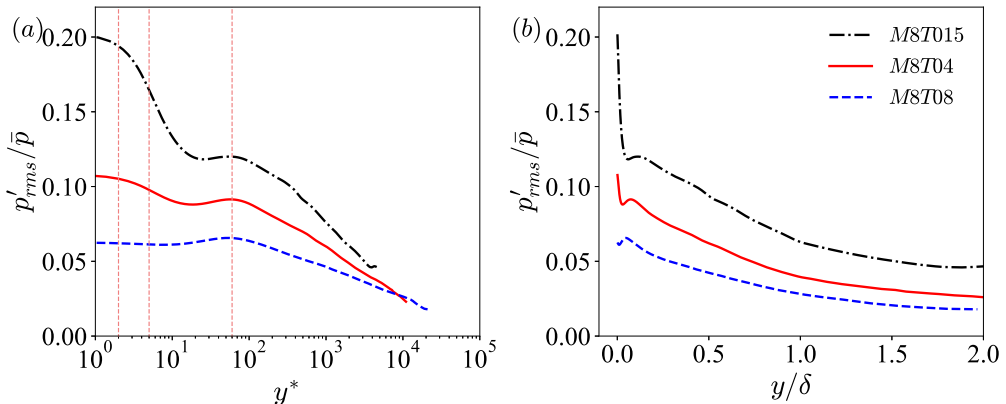


FIGURE 5. The normalised turbulent intensity of the pressure p'_{rms}/\bar{p} plotted against (a) semi-local scaling (y^*) and (b) outer scaling (y/δ). The vertical dashed lines represent $y^* = 2, 5, 60$ in (a).

The normalised turbulent intensity of the pressure p'_{rms}/\bar{p} along wall-normal direction is plotted in figure 5. It is found that the p'_{rms}/\bar{p} profile in nearly adiabatic wall case (“M8T08” case) reaches the maximum value at $y^* \approx 60$, and then decreases rapidly among the boundary layer to a flat platform. As the wall temperature decreases, the intensity of pressure p'_{rms}/\bar{p} significantly increases among the whole boundary layer. The profiles of p'_{rms}/\bar{p} in “M8T04” and “M8T015” have secondary peaks at $y^* \approx 60$, which are consistent with the wall-normal location of the primary peak in “M8T08”. A special phenomenon is observed that the intensities of p'_{rms}/\bar{p} are significantly enhanced near the wall when the wall is strongly cooled, which further result in the fact that the p'_{rms}/\bar{p} profiles attain their primary peaks at the wall in “M8T04” and “M8T015”. The significant enhancement of p'_{rms}/\bar{p} near the wall can be ascribed to the appearance of a special acoustic structure (“the travelling-wave-like alternating positive and negative structures” or TAPNS) in the near-wall region, which will be specifically discussed in Section 4.

The dimensionless entropy per unit mass s can be defined as $s = C_v \log(T/\rho^{\gamma-1})$ (Gerolymos & Vallet 2014; Wang *et al.* 2019). The normalised turbulent intensities $s'_{rms}\gamma M^2$, $\rho'_{rms}/\bar{\rho}$ and T'_{rms}/\bar{T} along wall-normal direction are shown in figure 6. It is found in figure 6 (a) and (d) that the normalised turbulent intensity of the entropy $s'_{rms}\gamma M^2$ attains its primary peak near the edge of the boundary layer ($y/\delta \approx 0.7$). Furthermore, a secondary peak is observed at $y^* \approx 50$ in “M8T08”, and this local secondary peak gradually disappears as the wall temperature decreases. It is also found that as the wall temperature decreases, the intensity $s'_{rms}\gamma M^2$ decreases in the region between $y^* > 10$ and $y/\delta < 0.7$, while $s'_{rms}\gamma M^2$ is significantly enhanced in the near-wall region ($y^* < 10$). An interesting phenomenon is found that a strong local secondary peak is observed at $y^* \approx 5$ in “M8T015”. It is noted that the local secondary peaks also appear in the near-wall region in “M6Tw025” and “M14Tw018” cases in Zhang *et al.* (2018). However, to the best of our knowledge, previous studies have not provided a physical explanation for the strong local secondary peak of $s'_{rms}\gamma M^2$ in the near-wall region when the wall is strongly cooled. In Section 4, it is found that the above phenomenon can be attributed to the appearance of a special entropic structure (“the streaky entropic structures” or SES) near the wall.

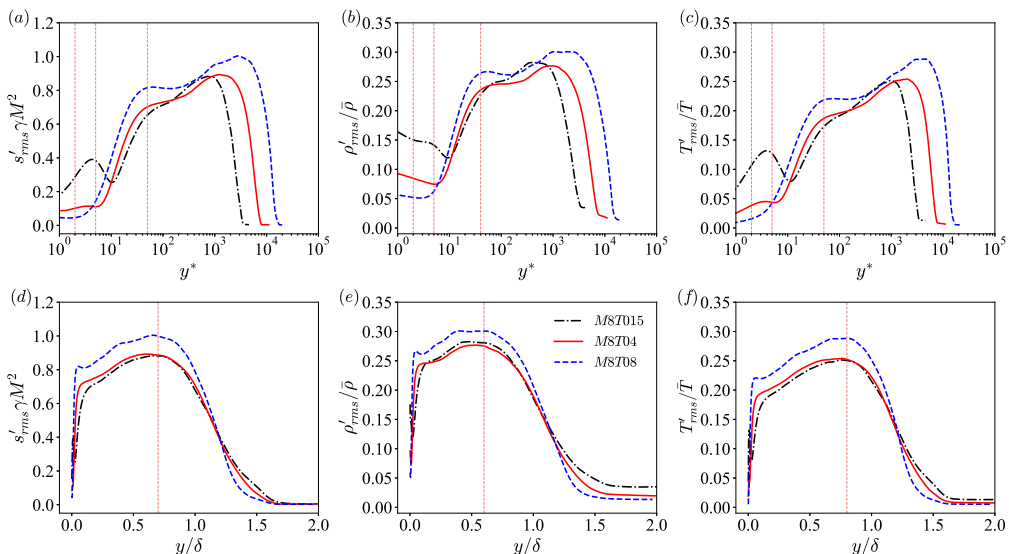


FIGURE 6. (a) and (d): The normalised turbulent intensity of the entropy $s'_{rms}\gamma M^2$ along wall-normal direction against (a) semi-local scaling (y^*) and (d) outer scaling (y/δ). The vertical dashed lines represent $y^* = 2, 5, 50$ in (a) and $y/\delta = 0.7$ in (d) respectively. (b) and (e): The normalised turbulent intensity of the density $\rho'_{rms}/\bar{\rho}$ along wall-normal direction against (b) semi-local scaling (y^*) and (e) outer scaling (y/δ). The vertical dashed lines represent $y^* = 2, 5, 40$ in (b) and $y/\delta = 0.6$ in (e) respectively. (c) and (f): The normalised turbulent intensity of the temperature T'_{rms}/\bar{T} along wall-normal direction against (c) semi-local scaling (y^*) and (f) outer scaling (y/δ). The vertical dashed lines represent $y^* = 2, 5, 50$ in (c) and $y/\delta = 0.8$ in (f) respectively.

It is also found that the intensities $\rho'_{rms}/\bar{\rho}$ and T'_{rms}/\bar{T} have similar behaviours with $s'_{rms}\gamma M^2$ among most regions of the boundary layer, except for the much larger values of $\rho'_{rms}/\bar{\rho}$ in the vicinity of the wall ($y^* < 5$). The similarity among the intensities $\rho'_{rms}/\bar{\rho}$, T'_{rms}/\bar{T} and $s'_{rms}\gamma M^2$ can be explained based on the Kovaszny decomposition (Kovaszny 1953; Chassaing *et al.* 2002; Gauthier 2017; Wang *et al.* 2019). It is noted that the Kovaszny decomposition can decompose the thermodynamic variables into the acoustic modes and the entropic modes (Kovaszny 1953; Chassaing *et al.* 2002; Gauthier 2017; Wang *et al.* 2019).

In compressible turbulent flow, the acoustic modes of the thermodynamic variables can be defined as (Chassaing *et al.* 2002; Gauthier 2017; Wang *et al.* 2019)

$$p'_I = p - \bar{p}, \quad (3.1)$$

$$\rho'_I = \frac{\bar{\rho} p'_I}{\gamma \bar{p}}, \quad (3.2)$$

$$T'_I = \frac{(\gamma - 1) \bar{T} p'_I}{\gamma \bar{p}}, \quad (3.3)$$

and the entropic modes can be given by (Chassaing *et al.* 2002; Gauthier 2017; Wang *et al.* 2019)

$$p'_E = 0, \quad (3.4)$$

$$\rho'_E = \rho - \bar{\rho} - \rho'_I, \quad (3.5)$$

$$T'_E = T - \bar{T} - T'_I. \quad (3.6)$$

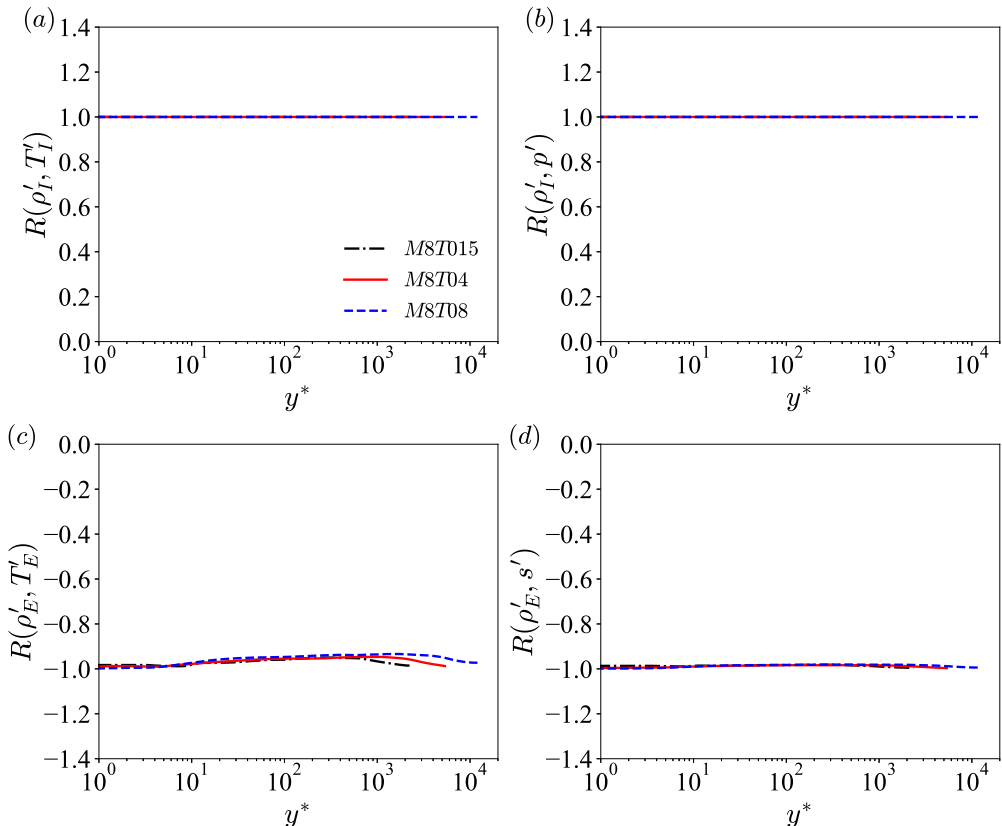


FIGURE 7. The correlation coefficients (a) $R(\rho'_I, T'_I)$, (b) $R(\rho'_I, p')$, (c) $R(\rho'_E, T'_E)$ and (d) $R(\rho'_E, s')$ along wall-normal direction plotted against semi-local scaling (y^*).

Therefore, the acoustic mode of the pressure p'_I is consistent with the fluctuating pressure p' , and the fluctuating density and temperature can be divided into the acoustic modes and the entropic modes respectively: $\rho' = \rho'_I + \rho'_E$; $T' = T'_I + T'_E$. It is noted that the correlation coefficients between variables φ' and ψ' can be defined as

$$R(\varphi', \psi') = \frac{\overline{\varphi' \psi'}}{\sqrt{\overline{\varphi'^2}} \sqrt{\overline{\psi'^2}}}. \quad (3.7)$$

The correlation coefficient $R(\varphi', \psi') = 1$ indicates that the variables φ' and ψ' are positively linearly correlated with each other; while $R(\varphi', \psi') = -1$ suggests that the variables φ' and ψ' are negatively linearly correlated with each other.

The correlation coefficients $R(\rho'_I, T'_I)$, $R(\rho'_I, p')$, $R(\rho'_E, T'_E)$ and $R(\rho'_E, s')$ along wall-normal direction are shown in figure 7. It is found that $R(\rho'_I, T'_I) = 1$ and $R(\rho'_I, p') = 1$ along wall-normal direction, confirming that ρ'_I , T'_I and p' are positively linearly correlated with each other. Furthermore, $R(\rho'_E, T'_E) \approx -1$ and $R(\rho'_E, s') \approx -1$, suggesting that ρ'_E is almost negatively linearly correlated with T'_E and s' respectively. Accordingly, the acoustic modes of density and temperature ρ'_I and T'_I are linearly correlated with the fluctuating pressure p' , and the entropic modes of density and temperature ρ'_E and T'_E are almost linearly correlated with the fluctuating entropy s' .

The normalised turbulent intensities of the acoustic and entropic modes of density

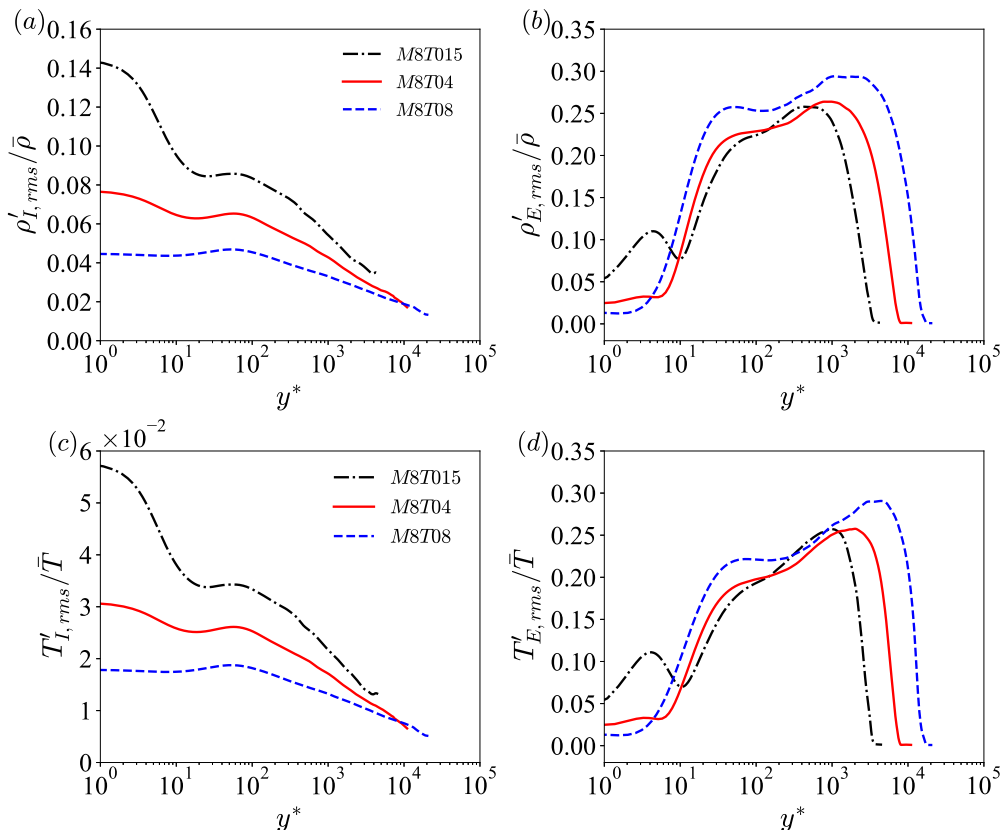


FIGURE 8. (a) and (b): The normalised turbulent intensity of (a) the acoustic mode of density $\rho'_{I,rms}/\bar{\rho}$ and (b) the entropic mode of density $\rho'_{E,rms}/\bar{\rho}$ along wall-normal direction. (c) and (d): The normalised turbulent intensity of (c) the acoustic mode of temperature $T'_{I,rms}/\bar{T}$ and (d) the entropic mode of temperature $T'_{E,rms}/\bar{T}$ along wall-normal direction.

and temperature along wall-normal direction are shown in figure 8. It is found that the profiles of the intensities of the acoustic modes of density and temperature (figure 8 (a) (c)) are similar to that of the fluctuating pressure (figure 5 (a)), and the intensities of the entropic modes of density and temperature (figure 8 (b) (d)) also have similar behaviours with that of the fluctuating entropy (figure 6 (a)).

The relative contributions $\rho'_{E,rms}/(\rho'_{E,rms} + \rho'_{I,rms})$ and $T'_{E,rms}/(T'_{E,rms} + T'_{I,rms})$ along wall-normal direction are shown in figure 9. It is noted that if the relative contributions $\rho'_{E,rms}/(\rho'_{E,rms} + \rho'_{I,rms})$ and $T'_{E,rms}/(T'_{E,rms} + T'_{I,rms})$ are lower than 0.5, the acoustic modes of density and temperature are predominant over their entropic modes; on the contrary, if the relative contributions are larger than 0.5, the entropic modes are dominant. It is found that the relative contributions $\rho'_{E,rms}/(\rho'_{E,rms} + \rho'_{I,rms})$ and $T'_{E,rms}/(T'_{E,rms} + T'_{I,rms})$ increase as the wall-normal location increases. Furthermore, the relative contribution $\rho'_{E,rms}/(\rho'_{E,rms} + \rho'_{I,rms})$ is totally smaller than $T'_{E,rms}/(T'_{E,rms} + T'_{I,rms})$ among the boundary layer, suggesting that the entropic mode has a much larger contribution in fluctuating temperature than that in fluctuating density. In the near-wall region, the fluctuating density is mainly dominated by its acoustic mode, and the acoustic mode of temperature is slightly predominant over the entropic mode of temperature. However, in the far-wall region,

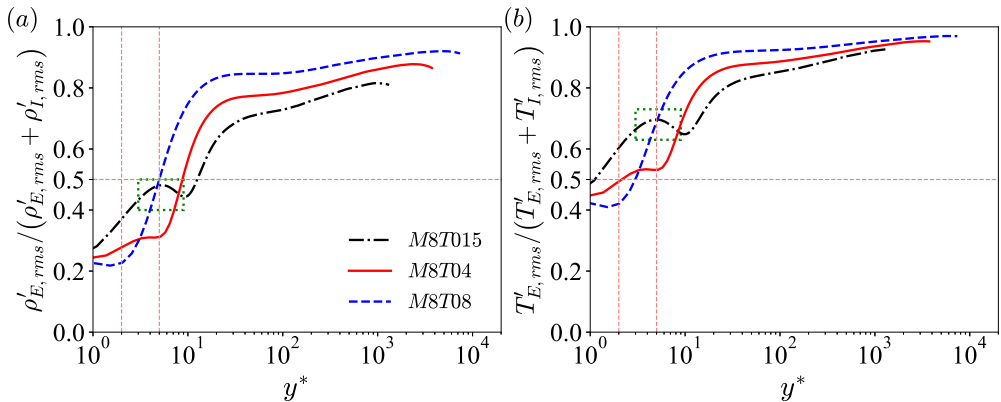


FIGURE 9. The relative contributions (a) $\rho'_{E,rms}/(\rho'_{E,rms} + \rho'_{I,rms})$ and (b) $T'_{E,rms}/(T'_{E,rms} + T'_{I,rms})$ along wall-normal direction. The vertical dashed lines represent $y^* = 2, 5$ in (a) and (b).

the fluctuating density and temperature are mainly dominated by their entropic modes, which further lead to the similarity between the profiles of $s'_{rms}\gamma M^2$, $\rho'_{rms}/\bar{\rho}$ and T'_{rms}/\bar{T} shown in figure 6.

It is also found that the wall temperature has a significant influence on the relative contributions. In the near-wall region, as the wall temperature decreases, the acoustic modes and the entropic modes of density and temperature are all enhanced, but the amounts of the growth of the entropic modes are slightly larger than those of the acoustic modes, which result in the increase of the relative contributions $\rho'_{E,rms}/(\rho'_{E,rms} + \rho'_{I,rms})$ and $T'_{E,rms}/(T'_{E,rms} + T'_{I,rms})$ with colder wall temperature. In the far-wall region, when the wall temperature becomes colder, the acoustic modes are enhanced while the entropic modes are reduced, which lead to the decrease of the relative contributions of the entropic modes in strongly cooled wall case. Therefore, as the wall temperature decreases, the increase of $\rho'_{rms}/\bar{\rho}$ and T'_{rms}/\bar{T} near the wall is mainly due to the contributions of both the acoustic and entropic modes, while the decrease of $\rho'_{rms}/\bar{\rho}$ and T'_{rms}/\bar{T} far from the wall can be ascribed to the major contributions of the entropic modes.

It has been noted previously in figure 6 (b) that $\rho'_{rms}/\bar{\rho}$ has much larger values than those of $s'_{rms}\gamma M^2$ and T'_{rms}/\bar{T} in the vicinity of the wall ($y^* < 5$), especially in “M8T04” and “M8T015”. This can be ascribed to the dominant contribution of the acoustic mode to the fluctuating density near the wall (figure 9 (a)), and the fact that the acoustic mode of density attains the primary peak at the wall in “M8T04” and “M8T015” (figure 8 (a)). Moreover, it is also found in figure 6 (e) that the primary peak value of $\rho'_{rms}/\bar{\rho}$ at $y/\delta \approx 0.6$ in “M8T015” is slightly larger than that in “M8T04”, which is opposite to the behaviours of $s'_{rms}\gamma M^2$ and T'_{rms}/\bar{T} . This can be attributed to the facts that the intensity of the acoustic mode of density in “M8T015” is much larger than that in “M8T04” (figure 8 (a)), and the acoustic mode of density in “M8T015” has a much larger contribution to fluctuating density than that in “M8T04” near the edge of the boundary layer (figure 9 (a)).

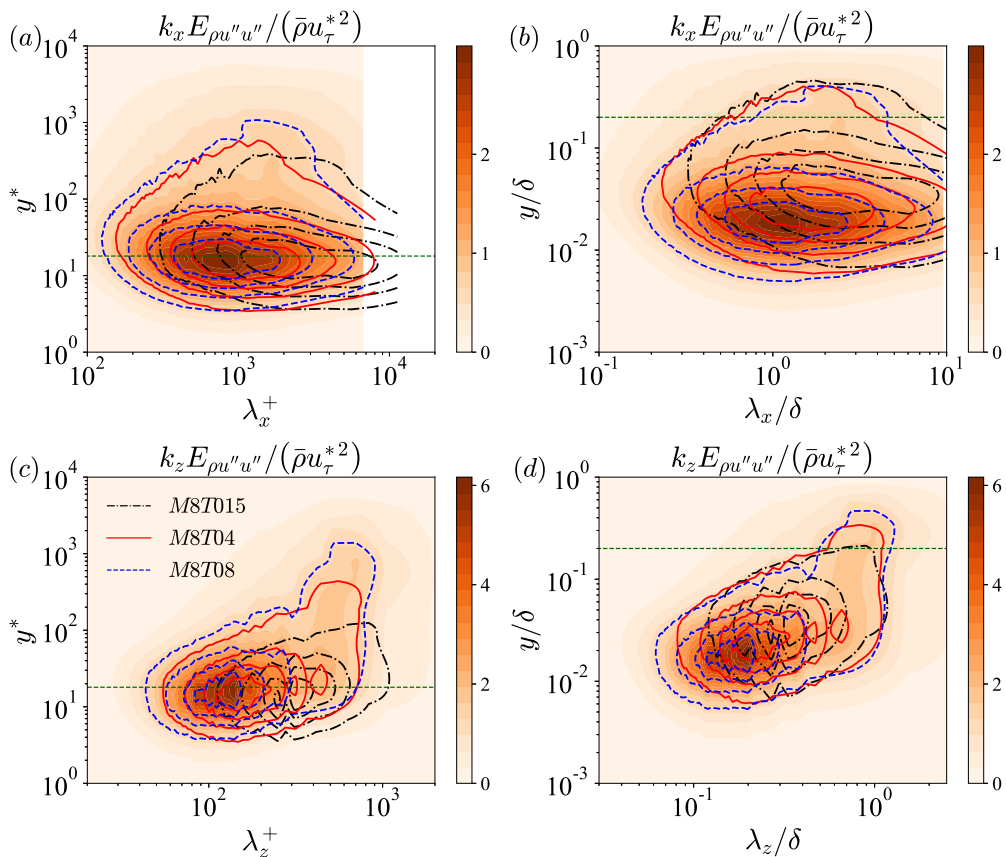


FIGURE 10. (a) and (b): The normalised premultiplied streamwise spectra of the fluctuating streamwise velocity $k_x E_{\rho u'' u''} / (\bar{\rho} u_\tau^{*2})$ in (a) inner scaling and (b) outer scaling. (c) and (d): The normalised premultiplied spanwise spectra of the fluctuating streamwise velocity $k_z E_{\rho u'' u''} / (\bar{\rho} u_\tau^{*2})$ in (c) inner scaling and (d) outer scaling. The filled contour represents the normalised premultiplied spectra in “M8T08”. The line contour levels are (0.2, 0.4, 0.6, 0.8) times the peak values. The horizontal dashed lines represent $y^* = 18$ in (a) (c) and $y/\delta = 0.2$ in (b) (d) respectively.

4. The streamwise and spanwise spectra of the streamwise velocity and thermodynamic variables

In order to quantitatively characterize the characteristic length scales of the energetic structures of the streamwise velocity and thermodynamic variables, the premultiplied streamwise and spanwise spectra are further investigated. It is noted that k_x and k_z are the wavenumber in the streamwise and spanwise directions respectively. λ_x and λ_z are the corresponding wavelength in the streamwise and spanwise directions respectively. Furthermore, $\lambda_x^+ = \lambda_x / \delta_\nu$ and $\lambda_x^* = \lambda_x / \delta_\nu^*$.

The normalised premultiplied streamwise and spanwise spectra of the fluctuating streamwise velocity $k_x E_{\rho u'' u''} / (\bar{\rho} u_\tau^{*2})$ and $k_z E_{\rho u'' u''} / (\bar{\rho} u_\tau^{*2})$ are shown in figure 10. It is found in figure 10 (a) and (c) that the premultiplied streamwise and spanwise spectra of the fluctuating streamwise velocity achieve their primary peaks at $y^* \approx 18$, which are consistent with the primary peak location of u''_{rms} / u_τ^* (figure 4 (a)). The peak of u''_{rms} / u_τ^* corresponds to the cycle of the near-wall streak generation (Jiménez & Pinelli

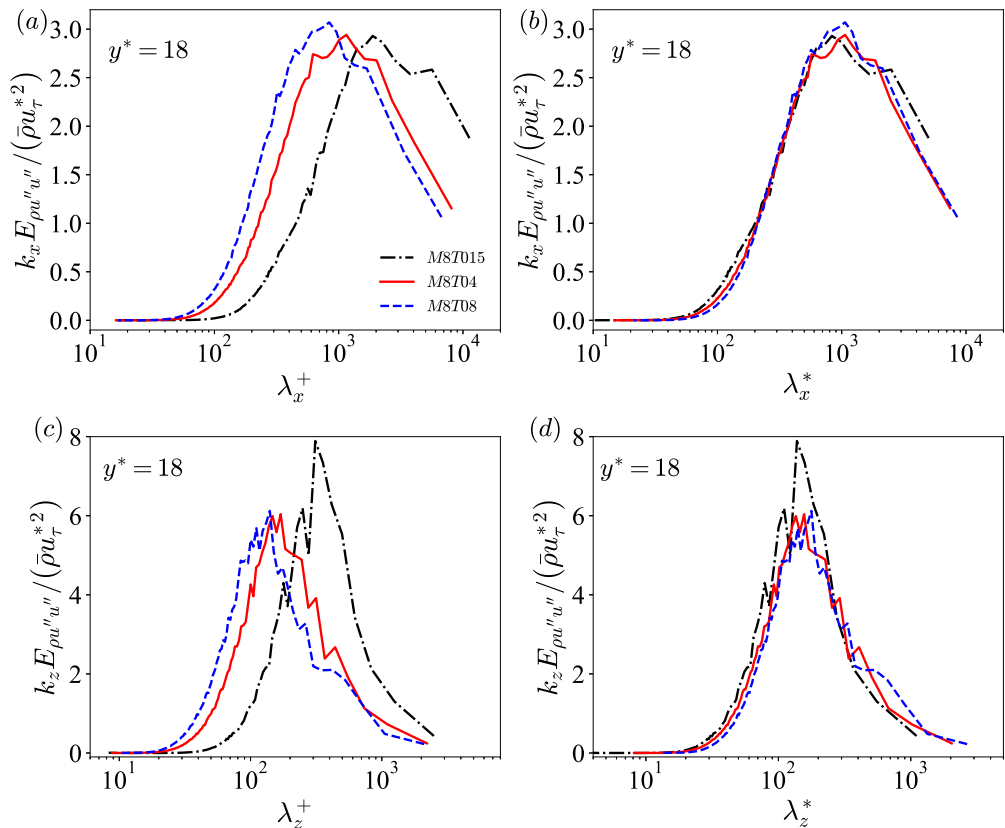


FIGURE 11. (a) and (b): The normalised premultiplied streamwise spectra of the fluctuating streamwise velocity $k_x E_{\rho u'' u''} / (\bar{\rho} u_\tau^{*2})$ at $y^* = 18$ plotted against (a) λ_x^+ and (b) λ_x^* . (c) and (d): The normalised premultiplied spanwise spectra of the fluctuating streamwise velocity $k_z E_{\rho u'' u''} / (\bar{\rho} u_\tau^{*2})$ at $y^* = 18$ plotted against (c) λ_z^+ and (d) λ_z^* .

1999; Jiménez 2013; Hutchins & Marusic 2007b; Monty *et al.* 2009; Pirozzoli & Bernardini 2013; Huang *et al.* 2022). Furthermore, $k_z E_{\rho u'' u''} / (\bar{\rho} u_\tau^{*2})$ has a weak outer peak at nearly $y/\delta \approx 0.2$ (figure 10 (d)), indicating the long streaky motion in the outer region (i.e. LSMs or VLSMs) (Hutchins & Marusic 2007a; Monty *et al.* 2009; Pirozzoli & Bernardini 2011, 2013; Hwang 2016; Huang *et al.* 2022). However, the outer peak of $k_x E_{\rho u'' u''} / (\bar{\rho} u_\tau^{*2})$ is not evident (figure 10 (b)), mainly due to the relatively low Reynolds number of the DNS database (Hwang 2016).

The normalised premultiplied streamwise and spanwise spectra of the fluctuating streamwise velocity $k_x E_{\rho u'' u''} / (\bar{\rho} u_\tau^{*2})$ and $k_z E_{\rho u'' u''} / (\bar{\rho} u_\tau^{*2})$ at $y^* = 18$ and $y/\delta = 0.2$ are shown in figure 11 and figure 12 respectively. It is found in figure 11 (a) and (c) that the peak locations of the premultiplied streamwise and spanwise spectra of the fluctuating streamwise velocity in wall unit (λ_x^+, λ_z^+) increase significantly as the wall temperature decreases, especially in strongly cooled wall case “M8T015”. These peak locations represent the characteristic streamwise length and spanwise spacing of the near-wall streaks. However, the semi-local scaling (λ_x^*, λ_z^*) can significantly reduce the disparity between the peak locations of spectra (figure 11 (b) (d)), yielding the characteristic streamwise length $\lambda_x^* \approx 10^3$ and spanwise spacing $\lambda_z^* \approx 150$ in different wall temperature cases. Similar values of the characteristic streamwise length and spanwise spacing of

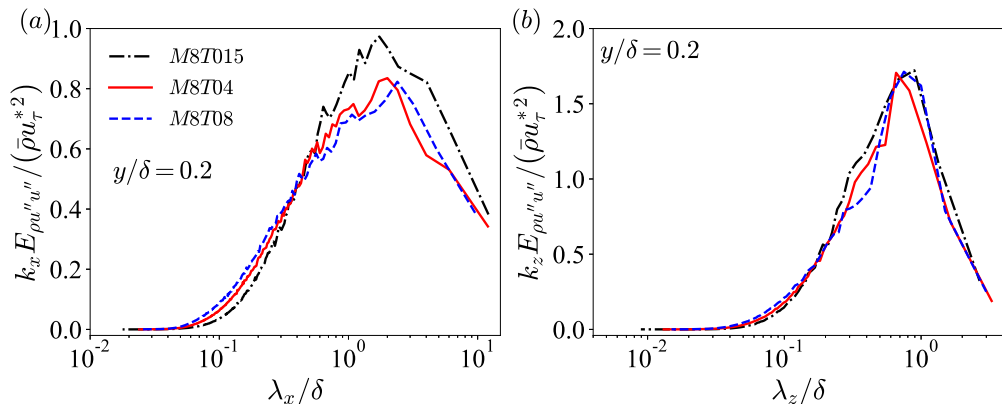


FIGURE 12. (a) The normalised premultiplied streamwise spectra of the fluctuating streamwise velocity $k_x E_{\rho u'' u''} / (\bar{\rho} u_\tau^{*2})$ at $y/\delta = 0.2$ plotted against λ_x/δ . (b) The normalised premultiplied spanwise spectra of the fluctuating streamwise velocity $k_z E_{\rho u'' u''} / (\bar{\rho} u_\tau^{*2})$ at $y/\delta = 0.2$ plotted against λ_z/δ .

the near-wall streaks have also been found in incompressible boundary layers (Hutchins & Marusic 2007b; Monty *et al.* 2009) and compressible boundary layers (Pirozzoli & Bernardini 2013; Huang *et al.* 2022). Furthermore, it is shown in figure 12 that the streamwise and spanwise spectra achieve their peak values at $\lambda_x/\delta \approx 2$ and $\lambda_z/\delta \approx 1$ respectively at $y/\delta = 0.2$, which represent the characteristic streamwise length and spanwise spacing of the long streaky motions in the outer region. Similar values of the characteristic spanwise spacing at $y/\delta = 0.2$ was also obtained in previous study of hypersonic turbulent boundary layers (Cogo *et al.* 2022).

The normalised premultiplied streamwise and spanwise spectra of the fluctuating pressure $k_x E_{p' p'} / \bar{p}^2$ and $k_z E_{p' p'} / \bar{p}^2$ are shown in figure 13. The $k_x E_{p' p'} / \bar{p}^2$ and $k_z E_{p' p'} / \bar{p}^2$ in the nearly adiabatic wall case “M8T08” achieve their primary peaks at $y^* \approx 60$, while the pressure spectra of “M8T04” and “M8T015” achieve their primary peaks at the wall. These observations are consistent with the primary peak locations of p'_{rms} / \bar{p} (figure 5 (a)).

The normalised premultiplied streamwise and spanwise spectra of the fluctuating pressure $k_x E_{p' p'} / \bar{p}^2$ and $k_z E_{p' p'} / \bar{p}^2$ at $y^* = 60$, $y^* = 2$ and $y^* = 5$ are shown in figure 14, figure 15 and figure 17 respectively. It is shown in figure 14 that as the wall temperature decreases, the peak values of $k_x E_{p' p'} / \bar{p}^2$ and $k_z E_{p' p'} / \bar{p}^2$ are drastically enhanced, and the peak locations also increase under the wall unit $(\lambda_x^+, \lambda_z^+)$ at $y^* = 60$. The semi-local scaling $(\lambda_x^*, \lambda_z^*)$ significantly reduces the disparity between the peak locations, and $k_x E_{p' p'} / \bar{p}^2$ and $k_z E_{p' p'} / \bar{p}^2$ achieve their peaks at $\lambda_x^* \approx 400$ and $\lambda_z^* \approx 250$ respectively at $y^* = 60$.

However, in the near-wall region ($y^* = 2$), the behaviours of the pressure spectra are quite different. It is found in figure 15 that peak locations of $k_x E_{p' p'} / \bar{p}^2$ and $k_z E_{p' p'} / \bar{p}^2$ in the nearly adiabatic wall case “M8T08” at $y^* = 2$ are significantly different from those in cooled wall cases “M8T04” and “M8T015”. This difference can be explained according to the instantaneous fields of the normalised fluctuating pressure p' / \bar{p} at $y^* = 2$ as shown in figure 16. It is shown in figure 16 (a) and (b) that the special structures marked by red dashed boxes are observed, and these structures are named as “the travelling-wave-like alternating positive and negative structures” (TAPNS). These structures are well organized as wavelike alternating positive and negative patterns along the streamwise

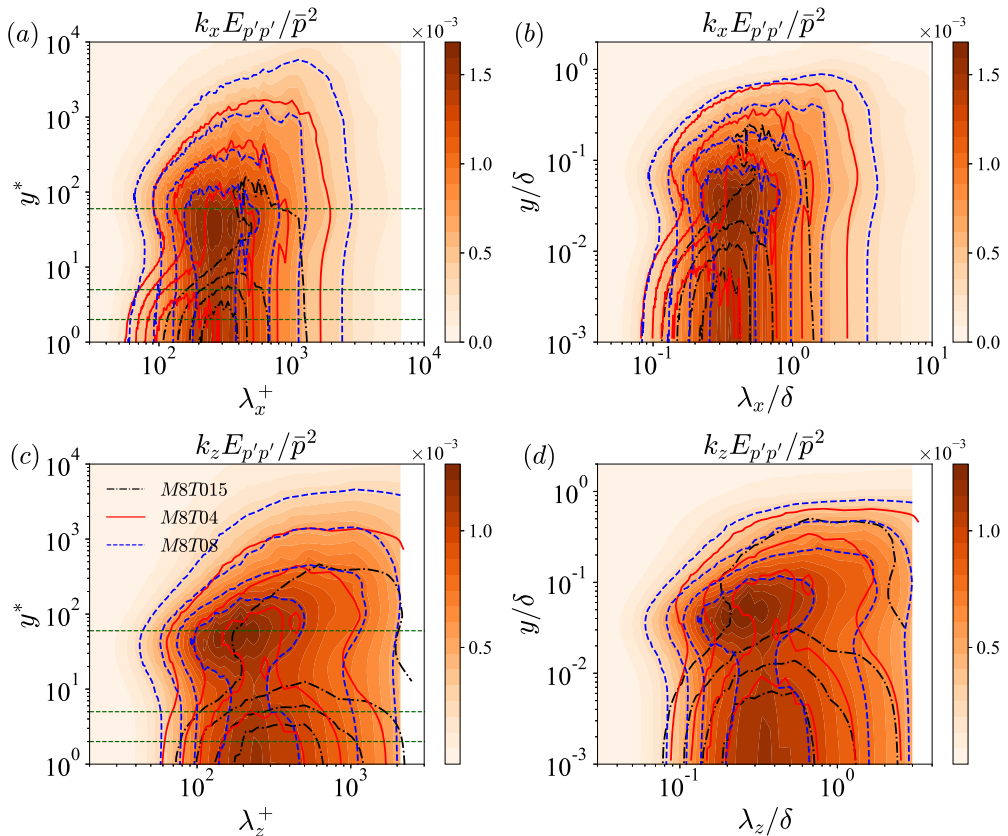


FIGURE 13. (a) and (b): The normalised premultiplied streamwise spectra of the fluctuating pressure $k_x E_{p'p'} / \bar{p}^2$ in (a) inner scaling and (b) outer scaling. (c) and (d): The normalised premultiplied spanwise spectra of the fluctuating pressure $k_z E_{p'p'} / \bar{p}^2$ in (c) inner scaling and (d) outer scaling. The filled contour represents the normalised premultiplied spectra in “M8T08”. The line contour levels are (0.2, 0.4, 0.6, 0.8) times the peak values. The horizontal dashed lines represent $y^* = 2, 5, 60$ in (a) (c).

direction, and have also been found in compressible channel flows (Yu *et al.* 2019; Tang *et al.* 2020) and turbulent boundary layers (Xu *et al.* 2021b; Zhang *et al.* 2022). Moreover, the TAPNS disappear in nearly adiabatic wall case “M8T08”, and are strongly enhanced as wall temperature decreases. Particularly, in the strongly cooled wall case “M8T015” (figure 16 (a)), the TAPNS are prevalent in the whole field. The extreme positive and negative values of p'/\bar{p} are mainly located among the TAPNS, which further lead to the significant enhancement of p'_{rms}/\bar{p} near the wall (figure 5 (a)). The peak locations of $k_x E_{p'p'} / \bar{p}^2$ and $k_z E_{p'p'} / \bar{p}^2$ in the nearly adiabatic wall case “M8T08” are $\lambda_x^* \approx 300$ and $\lambda_z^* \approx 200$ respectively at $y^* = 2$, which have similar aspect ratio $\lambda_x^* / \lambda_z^*$ to the characteristic scales at $y^* = 60$. Nevertheless, the pressure spectra achieve their peaks at $\lambda_x^* \approx 120$ and $\lambda_z^* \approx 200$ in “M8T04”, and $\lambda_x^* \approx 210$ and $\lambda_z^* \approx 250$ in “M8T015”. As the wall temperature decreases from “M8T04” to “M8T015”, the characteristic streamwise length scale λ_x^* is significantly increased, while the characteristic spanwise spacing scale λ_z^* is slightly enhanced, which is similar to the behaviour of the instantaneous wavelike alternating positive and negative structures shown in figure 16 (a) and (b). Therefore, it can be inferred that the characteristic streamwise length scale λ_x^* and spanwise

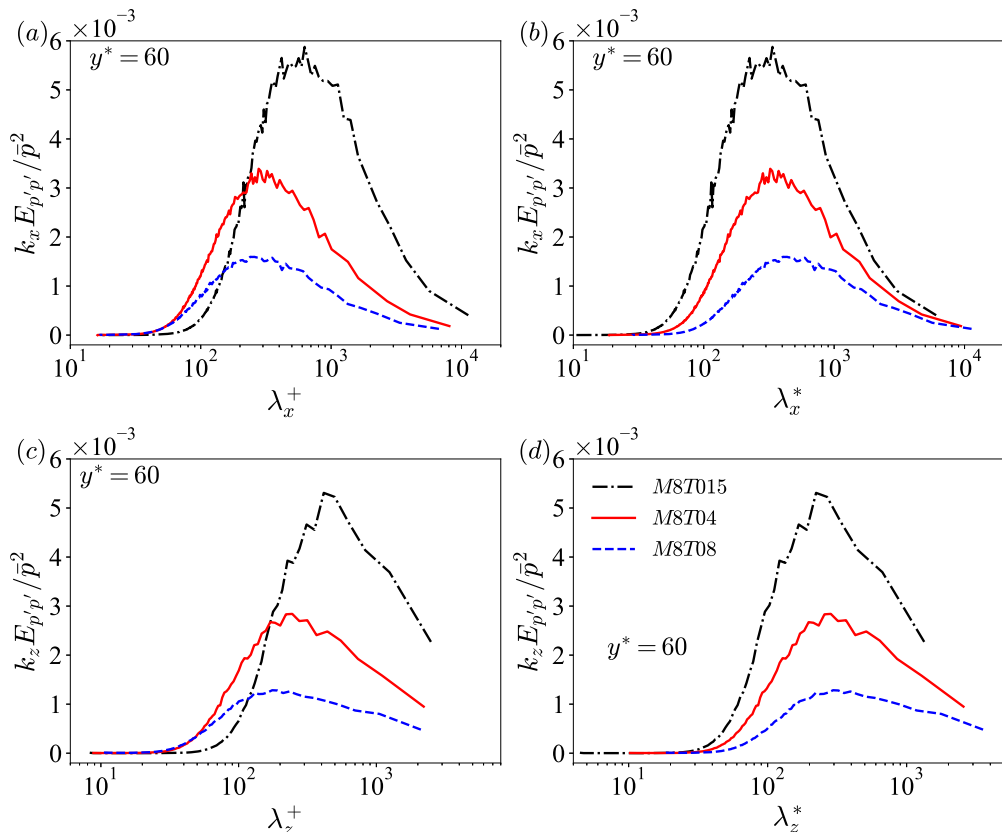


FIGURE 14. (a) and (b): The normalised premultiplied streamwise spectra of the fluctuating pressure $k_x E_{p'p'}/\bar{p}^2$ at $y^* = 60$ plotted against (a) λ_x^+ and (b) λ_x^* . (c) and (d): The normalised premultiplied spanwise spectra of the fluctuating pressure $k_z E_{p'p'}/\bar{p}^2$ at $y^* = 60$ plotted against (c) λ_z^+ and (d) λ_z^* .

spacing scale λ_z^* of the cooled wall cases “M8T04” and “M8T015” represent the scales of the TAPNS. The TAPNS is short and fat (i.e. $\lambda_x^* < \lambda_z^*$). As the wall temperature decreases, the aspect ratio λ_x^*/λ_z^* of TAPNS increases from almost 0.6 in “M8T04” to 0.84 in “M8T015”, which indicates that the strongly cooled wall prefers to increase the streamwise length scale compared with the spanwise spacing scale of TAPNS. Moreover, the intensity of the TAPNS is strongly enhanced as the wall temperature decreases. It is noted that these wavelike alternating positive and negative patterns have also been reported in the fluctuating dilatation $\theta'' \equiv \partial u_k''/\partial x_k$ in figure 6 of Xu *et al.* (2021b). Therefore, it can be deduced that as the wall temperature decreases, the peak values of the pressure spectra and the turbulent intensities of the pressure are significantly enhanced in the near-wall region, which further lead to the enhanced compressibility near the wall (Duan *et al.* 2010; Zhang *et al.* 2018; Xu *et al.* 2021a,b; Zhang *et al.* 2022). Moreover, it is shown above in figure 5 (a) that the maximum values of p'/\bar{p} appear at the wall in “M8T04” and “M8T015”. This phenomenon is attributed to the appearance of TAPNS near the wall in the cooled wall cases.

As the wall-normal location moves further away from the wall (at $y^* = 5$), it is shown in figure 17 that most of the peak locations of the streamwise and spanwise spectra are similar to those at $y^* = 2$, except for the peak location of $k_x E_{p'p'}/\bar{p}^2$ in “M8T04”.

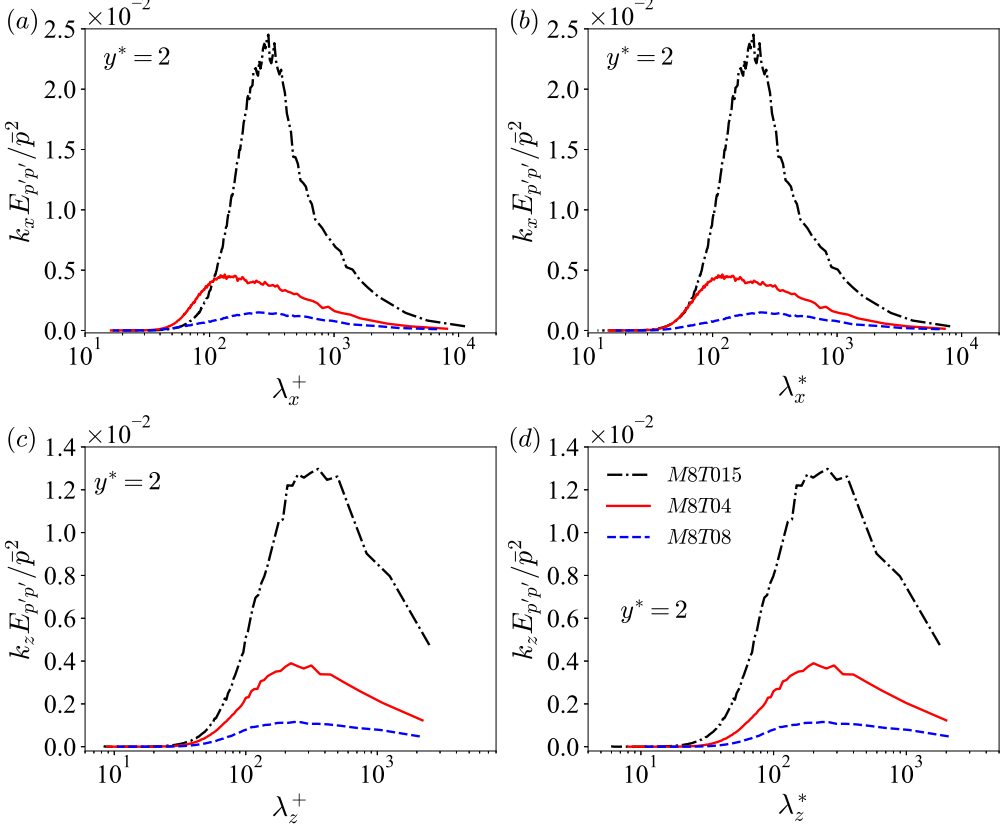


FIGURE 15. (a) and (b): The normalised premultiplied streamwise spectra of the fluctuating pressure $k_x E_{p'p'} / \bar{p}^2$ at $y^* = 2$ plotted against (a) λ_x^+ and (b) λ_x^* . (c) and (d): The normalised premultiplied spanwise spectra of the fluctuating pressure $k_z E_{p'p'} / \bar{p}^2$ at $y^* = 2$ plotted against (c) λ_z^+ and (d) λ_z^* .

It is found in figure 17 (b) that the peak of $k_x E_{p'p'} / \bar{p}^2$ in “M8T04” becomes much wider than that at $y^* = 2$, and the characteristic streamwise length scale of $k_x E_{p'p'} / \bar{p}^2$ in “M8T08” ($\lambda_x^* \approx 300$) is also found in the streamwise spectra in “M8T04”. Here for better description, the pressure structures with the characteristic streamwise length scale in “M8T08” are named as “the base acoustic structures”. The above observation indicates that the base acoustic structures also exist in the cooled wall cases “M8T04” and “M8T015”. If the wall is significantly cooled and the wall-normal location y^* is close to the wall, the strength of the TAPNS is much larger than that of the base pressure structures, and only the characteristic streamwise length scale λ_x^* of TAPNS is dominant in $k_x E_{p'p'} / \bar{p}^2$ (i.e. “M8T04” and “M8T015” in figure 15 (b) and “M8T015” in figure 17 (b)). As the wall temperature increases and y^* moves away from the wall, the intensity of the TAPNS becomes weaker. Therefore, the TAPNS and the base acoustic structures have similar intensities in these situations, which result in the wide peak in “M8T04” in figure 17 (b). When the wall temperature is nearly adiabatic (i.e. “M8T08”), the TAPNS disappear and only the base acoustic structures are dominant in the near-wall region.

The normalised premultiplied streamwise and spanwise spectra of the fluctuating entropy $k_x E_{s's'} (\gamma M^2)^2$ and $k_z E_{s's'} (\gamma M^2)^2$ are depicted in figure 18. The $k_x E_{s's'} (\gamma M^2)^2$ and $k_z E_{s's'} (\gamma M^2)^2$ achieve their primary peaks near the edge of the boundary layer,

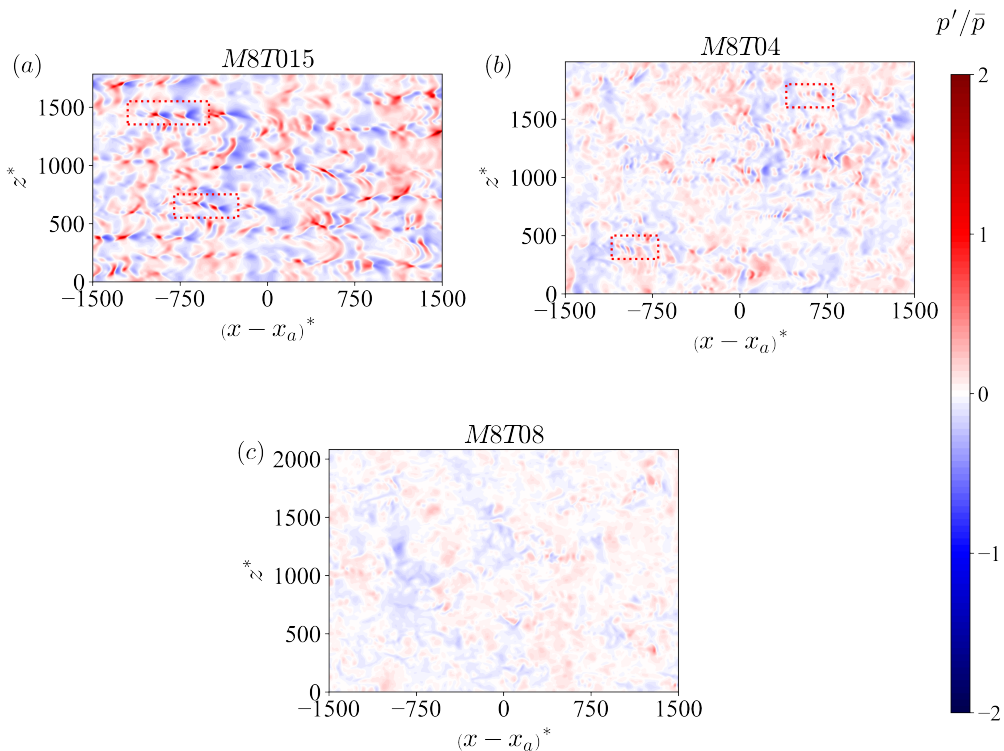


FIGURE 16. The instantaneous fields of the normalised fluctuating pressure p'/\bar{p} at $y^* = 2$ in (a) “M8T015”, (b) “M8T04” and (c) “M8T08”.

which are consistent with the primary peak location of $s'_{rms}\gamma M^2$ (figure 6 (d)). The secondary peaks of entropy spectra appear at $y^* \approx 50$ in “M8T08” and “M8T04”, which are coincident with the secondary peak location of $s'_{rms}\gamma M^2$ (figure 6 (a)). However, for the strongly cooled wall case “M8T015”, the secondary peaks of entropy spectra appear at nearly $y^* = 5$. The normalised premultiplied streamwise and spanwise spectra of the fluctuating entropy $k_x E_{s's'} (\gamma M^2)^2$ and $k_z E_{s's'} (\gamma M^2)^2$ at $y/\delta = 0.7$, $y^* = 50$, $y^* = 2$ and $y^* = 5$ are plotted in figure 19, figure 20, figure 21 and figure 23 respectively. It is shown in figure 19 that $k_x E_{s's'} (\gamma M^2)^2$ and $k_z E_{s's'} (\gamma M^2)^2$ attain their peaks at $\lambda_x/\delta \approx 1.3$ and $\lambda_z/\delta \approx 1$ respectively. Furthermore, the peak values of $k_x E_{s's'} (\gamma M^2)^2$ and $k_z E_{s's'} (\gamma M^2)^2$ decrease as the wall temperature decreases. It can be seen in figure 20 that the semi-local scaling can reduce the disparity between the peak locations of spectra. The $k_x E_{s's'} (\gamma M^2)^2$ and $k_z E_{s's'} (\gamma M^2)^2$ achieve their peaks at $\lambda_x^* \approx 700$ and $\lambda_z^* \approx 250$ respectively at $y^* = 50$. Furthermore, the peak values of the normalised premultiplied streamwise and spanwise spectra of the fluctuating entropy decrease as the wall temperature decreases, which are consistent with the observation that the values of $s'_{rms}\gamma M^2$ decrease as the wall temperature decreases at $y^* = 50$ (figure 6 (a)).

It is shown in figure 6 (a) that a local secondary peak of $s'_{rms}\gamma M^2$ appears near the wall in “M8T015”. The underlying mechanism of this phenomenon is revealed as follows. It is found in figure 21 that the peak values of the entropy spectra in “M8T04” and “M8T015” are significantly larger than those in “M8T08”, and the peak values increase as the wall temperature decreases. Furthermore, the $k_x E_{s's'} (\gamma M^2)^2$ in “M8T015” and

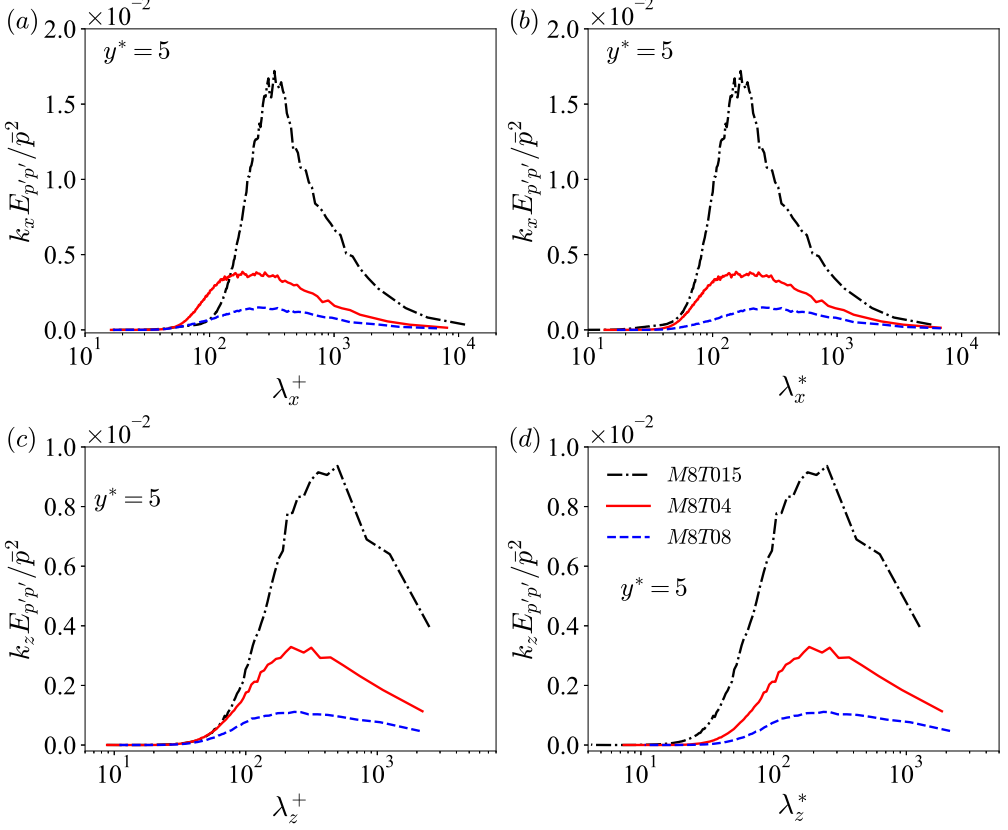


FIGURE 17. (a) and (b): The normalised premultiplied streamwise spectra of the fluctuating pressure $k_x E_{p'p'}/\bar{p}^2$ at $y^* = 5$ plotted against (a) λ_x^+ and (b) λ_x^* . (c) and (d): The normalised premultiplied spanwise spectra of the fluctuating pressure $k_z E_{p'p'}/\bar{p}^2$ at $y^* = 5$ plotted against (c) λ_z^+ and (d) λ_z^* .

“M8T04” attain their peaks at $\lambda_x/\delta \approx 2.3$ and 1.3 respectively, and the peak locations of the $k_z E_{s's'} (\gamma M^2)^2$ in “M8T015” and “M8T04” are $\lambda_z/\delta \approx 0.25$ and 0.2 respectively. The underlying structures of the characteristic scales of the entropy spectra are revealed by the instantaneous fields of the normalised fluctuating entropy $s'\gamma M^2$ at $y^* = 2$ shown in figure 22. It can be seen in figure 22 (a) and (b) that the long and thin fluctuating entropy structures only appear when the wall is cooled (“M8T015” and “M8T04”). These special entropic structures exhibit the streaky patterns with alternating stripes of the high and low entropy, which is similar to the streaks of u' (shown in figure 5 (a) in Xu *et al.* (2021a)) with $R(s', u') = 0.93$ at $y^* = 2$ in “M8T015”. However, the entropy structures in the nearly adiabatic wall case “M8T08” are pretty weak and fragmented. Here for the sake of description, the entropy structures in “M8T08” are named as “the base entropic structures”, while the generated streaky patterns in “M8T04” and “M8T015” are called “the streaky entropic structures” (SES). It is shown in figure 18 that the characteristic length scale is significantly larger than the characteristic spanwise spacing scale (i.e. $\lambda_x/\delta \gg \lambda_z/\delta$) in “M8T015” and “M8T04”, which is consistent with the long and thin nature of SES. Furthermore, the λ_x/δ and λ_z/δ in “M8T015” are larger than those in “M8T04”, which is coincident with the observation that the SES become longer in the streamwise direction and fatter in the spanwise direction as the wall temperature

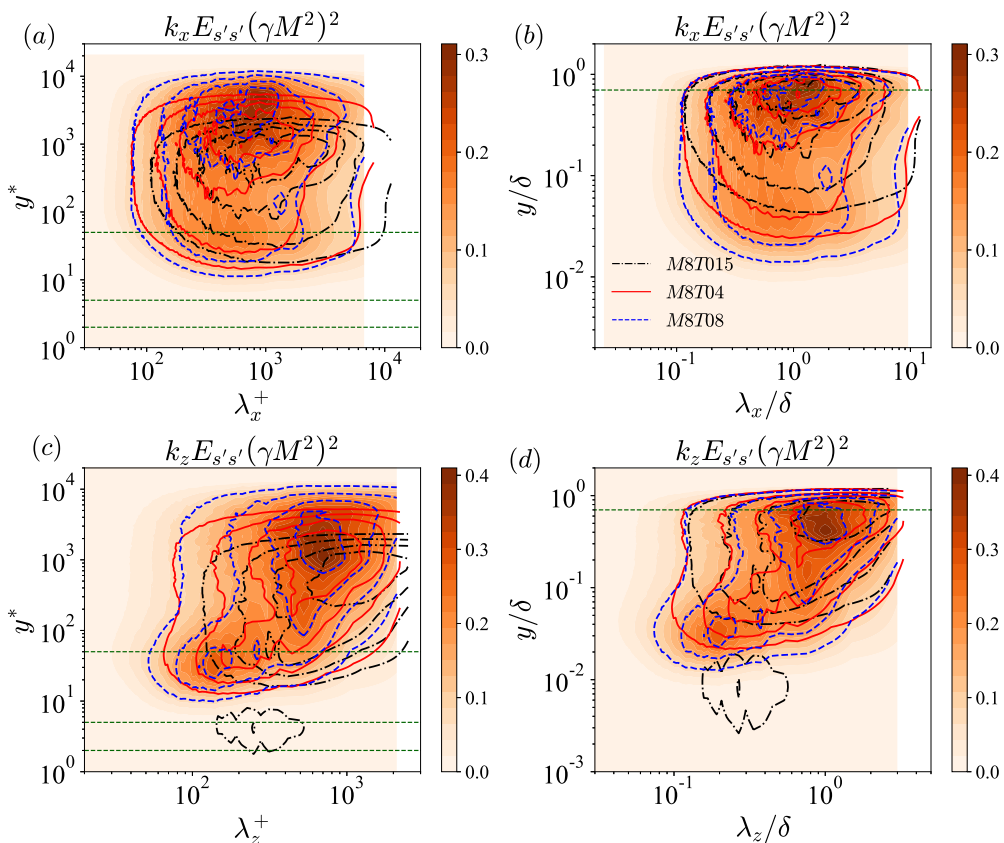


FIGURE 18. (a) and (b): The normalised premultiplied streamwise spectra of the fluctuating entropy $k_x E_{s's'} (\gamma M^2)^2$ in (a) inner scaling and (b) outer scaling. (c) and (d): The normalised premultiplied spanwise spectra of the fluctuating entropy $k_z E_{s's'} (\gamma M^2)^2$ in (c) inner scaling and (d) outer scaling. The filled contour represents the normalised premultiplied spectra in “M8T08”. The line contour levels are (0.2, 0.4, 0.6, 0.8) times the peak values. The horizontal dashed lines represent $y^* = 2, 5, 50$ in (a) (c) and $y/\delta = 0.7$ in (b) (d) respectively.

decreases (figure 22 (a) and (b)). Accordingly, it can be inferred that the characteristic streamwise length scale λ_x/δ and spanwise spacing scale λ_z/δ of the entropy spectra in “M8T015” and “M8T04” represent the scales of the SES. Furthermore, the aspect ratio λ_x/λ_z of SES increases from 6.5 in “M8T04” to 9.2 in “M8T015”, suggesting that the strongly cooled wall prefers to increase the streamwise length scale compared with the spanwise spacing scale of SES. Moreover, the intensity of the SES is significantly enhanced as the wall temperature decreases, which further leads to the significant enhancement of $s'_{rms} \gamma M^2$ near the wall in the cooled wall cases (figure 6 (a)). Specifically, the local secondary peak of $s'_{rms} \gamma M^2$ near the wall in “M8T015” is attributed to the strong intensity of the SES.

As the wall-normal location increases to $y^* = 5$, it is seen in figure 23 that the entropy spectra in “M8T08” and “M8T04” have pretty small peak values, and attain their peaks at $\lambda_x^* \approx 450$ and $\lambda_z^* \approx 140$ respectively at $y^* = 5$, which have a similar characteristic aspect ratio λ_x^*/λ_z^* with the characteristic scales at $y^* = 50$. Furthermore, the peak values of the entropy spectra in “M8T08” and “M8T04” decrease as the wall temperature decreases, which are coincident with the behaviours at $y^* = 50$ and $y/\delta = 0.7$. However,

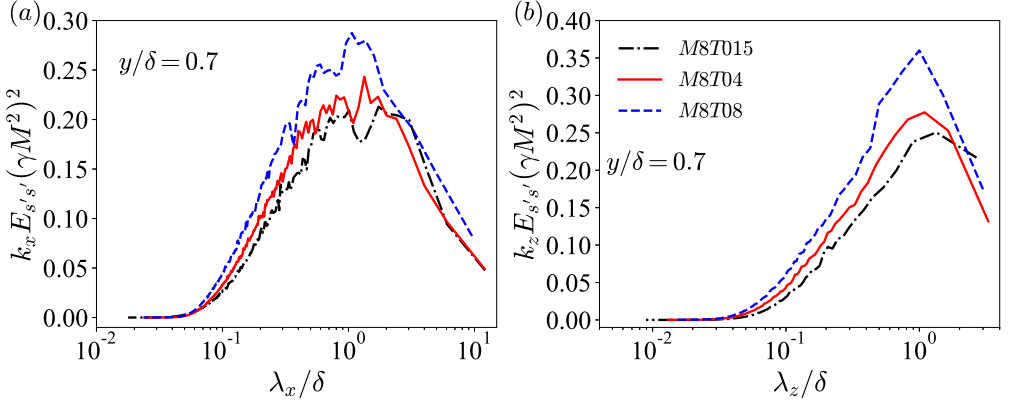


FIGURE 19. (a) The normalised premultiplied streamwise spectra of the fluctuating entropy $k_x E_{s's'} (\gamma M^2)^2$ at $y/\delta = 0.7$ plotted against λ_x/δ . (b) The normalised premultiplied spanwise spectra of the fluctuating entropy $k_z E_{s's'} (\gamma M^2)^2$ at $y/\delta = 0.7$ plotted against λ_z/δ .

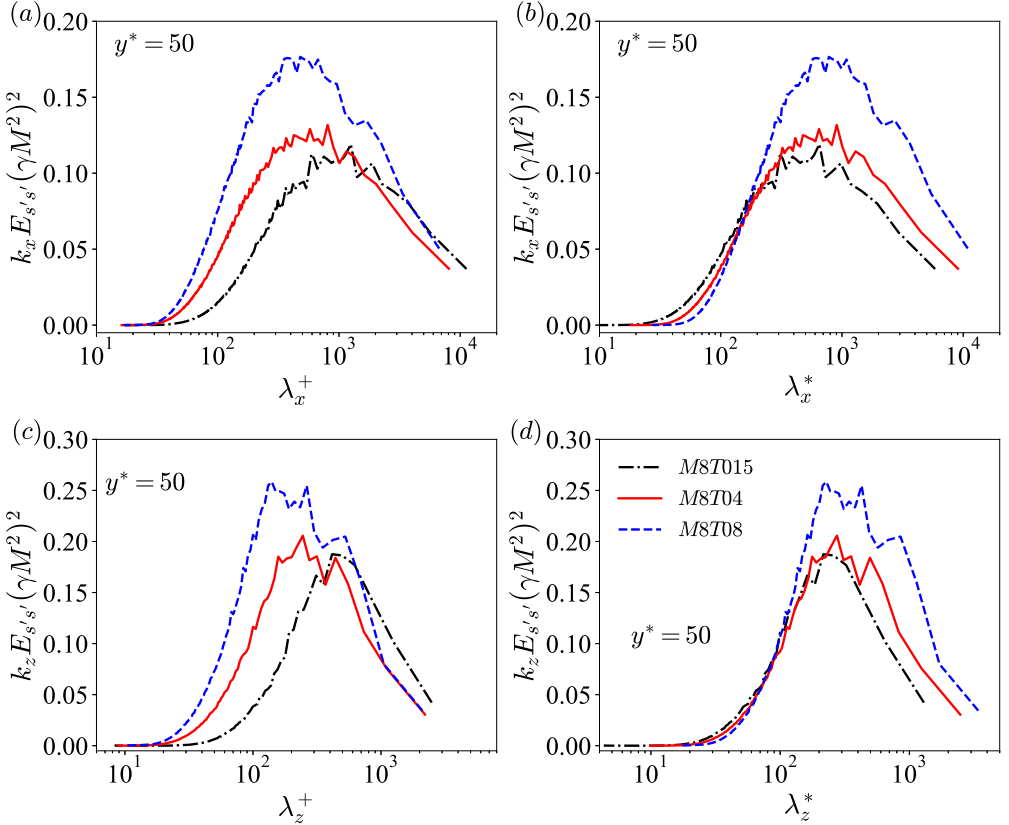


FIGURE 20. (a) and (b): The normalised premultiplied streamwise spectra of the fluctuating entropy $k_x E_{s's'} (\gamma M^2)^2$ at $y^* = 50$ plotted against (a) λ_x^+ and (b) λ_x^* . (c) and (d): The normalised premultiplied spanwise spectra of the fluctuating entropy $k_z E_{s's'} (\gamma M^2)^2$ at $y^* = 50$ plotted against (c) λ_z^+ and (d) λ_z^* .

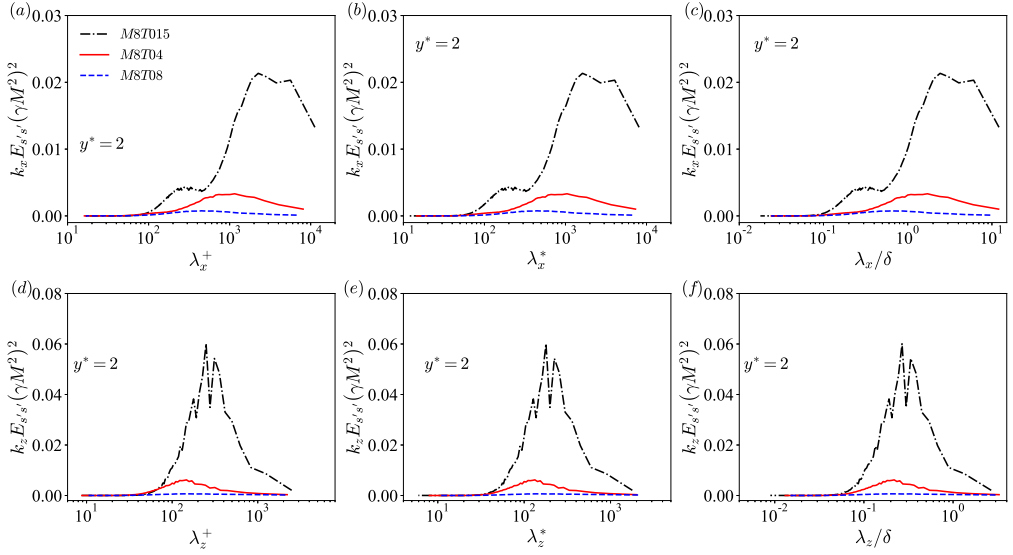


FIGURE 21. (a), (b) and (c): The normalised pre-multiplied streamwise spectra of the fluctuating entropy $k_x E_{s's'} (\gamma M^2)^2$ at $y^* = 2$ plotted against (a) λ_x^+ , (b) λ_x^* and (c) λ_x/δ . (d), (e) and (f): The normalised pre-multiplied spanwise spectra of the fluctuating entropy $k_z E_{s's'} (\gamma M^2)^2$ at $y^* = 2$ plotted against (d) λ_z^+ , (e) λ_z^* and (f) λ_z/δ .

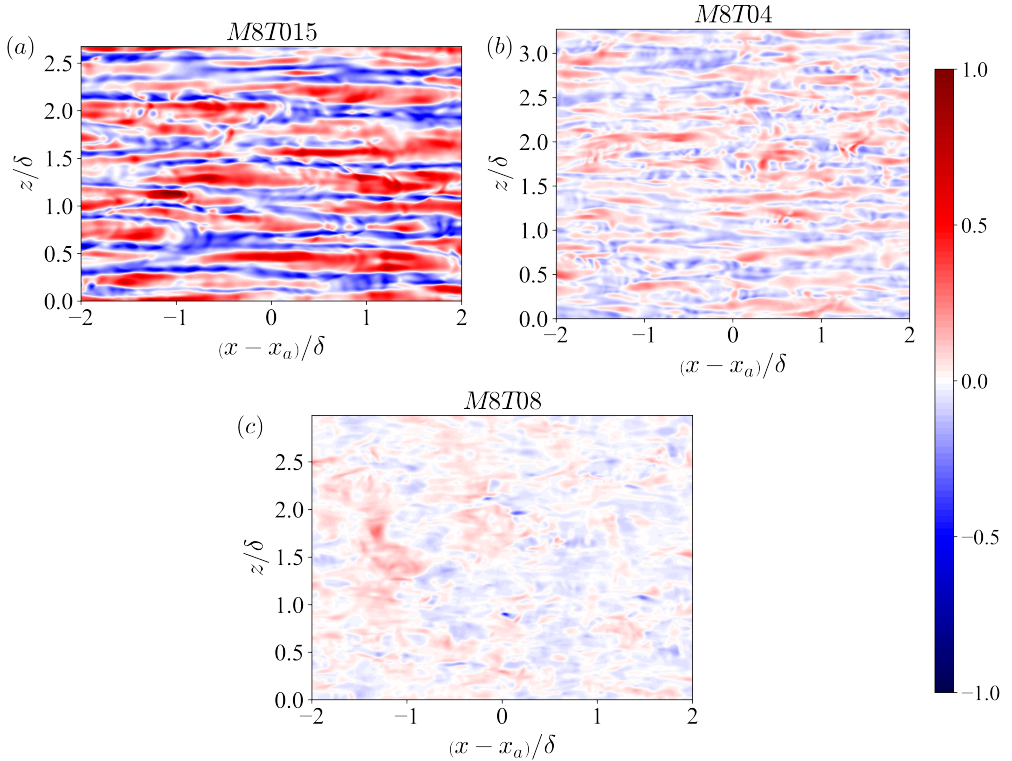


FIGURE 22. The instantaneous fields of the normalised fluctuating entropy $s' \gamma M^2$ at $y^* = 2$ in (a) “M8T015”, (b) “M8T04” and (c) “M8T08”.

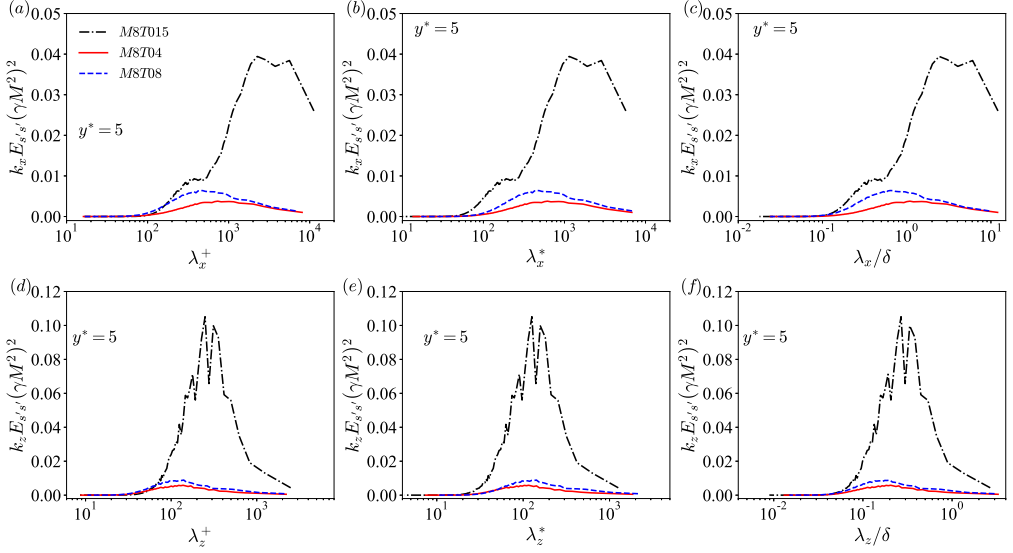


FIGURE 23. (a), (b) and (c): The normalised premultiplied streamwise spectra of the fluctuating entropy $k_x E_{s's'} (\gamma M^2)^2$ at $y^* = 5$ plotted against (a) λ_x^+ , (b) λ_x^* and (c) λ_x/δ . (d), (e) and (f): The normalised premultiplied spanwise spectra of the fluctuating entropy $k_z E_{s's'} (\gamma M^2)^2$ at $y^* = 5$ plotted against (d) λ_z^+ , (e) λ_z^* and (f) λ_z/δ .

the peak values of the entropy spectra in strongly cooled wall case “M8T015” are significantly larger than those in other two cases. The entropy spectra in “M8T015” attain their peaks at $\lambda_x/\delta \approx 2.3$ and $\lambda_z/\delta \approx 0.25$ respectively, which are similar to the characteristic scales at $y^* = 2$. The above observations indicate that the SES exist in “M8T015”, while disappear in “M8T04” at $y^* = 5$. Therefore, it is implied that the SES can exist in a larger range of wall-normal distance y^* as the wall temperature decreases.

The normalised premultiplied streamwise and spanwise spectra of the fluctuating density $k_x E_{\rho'\rho'}/\bar{\rho}^2$ and $k_z E_{\rho'\rho'}/\bar{\rho}^2$ are shown in figure 24. It is found that the spectra of the fluctuating density are similar to those of the fluctuating entropy at $y^* > 20$, which is consistent with the observation in figure 9 (a) that the fluctuating density is dominated by its entropic mode at $y^* > 20$. The $k_x E_{\rho'\rho'}/\bar{\rho}^2$ and $k_z E_{\rho'\rho'}/\bar{\rho}^2$ in three cases achieve their primary peaks at $y/\delta \approx 0.6$, and the secondary peak locations of the density spectra in “M8T08” and “M8T04” are $y^* \approx 40$, which are coincident with peak locations of $\rho'_{rms}/\bar{\rho}$ (figure 6 (b) (e)). However, a complicated behaviour of the density spectra appears in “M8T015”, mainly due to the strong variation of the relative contribution $\rho'_{E,rms}/(\rho'_{E,rms} + \rho'_{I,rms})$ at $y^* < 20$ with strongly cooled wall (figure 9 (a)).

The normalised premultiplied streamwise and spanwise spectra of the fluctuating density $k_x E_{\rho'\rho'}/\bar{\rho}^2$ and $k_z E_{\rho'\rho'}/\bar{\rho}^2$ at $y/\delta = 0.6$ and $y^* = 40$ are depicted in figure 25 and figure 26 respectively. The $k_x E_{\rho'\rho'}/\bar{\rho}^2$ and $k_z E_{\rho'\rho'}/\bar{\rho}^2$ achieve their peaks at $\lambda_x/\delta \approx 1.3$ and $\lambda_z/\delta \approx 1$ respectively at $y/\delta = 0.6$ (figure 25), and the peak locations of the density spectra are $\lambda_x^* \approx 700$ and $\lambda_z^* \approx 250$ respectively at $y^* = 40$ (figure 26). It is noted that the peak locations of the density spectra are totally similar to those of the entropy spectra (figure 19 and 20), which are mainly due to the reason that the fluctuating density is dominated by its entropic mode at $y^* > 20$ (figure 9 (a)).

The normalised premultiplied streamwise and spanwise spectra of the fluctuating

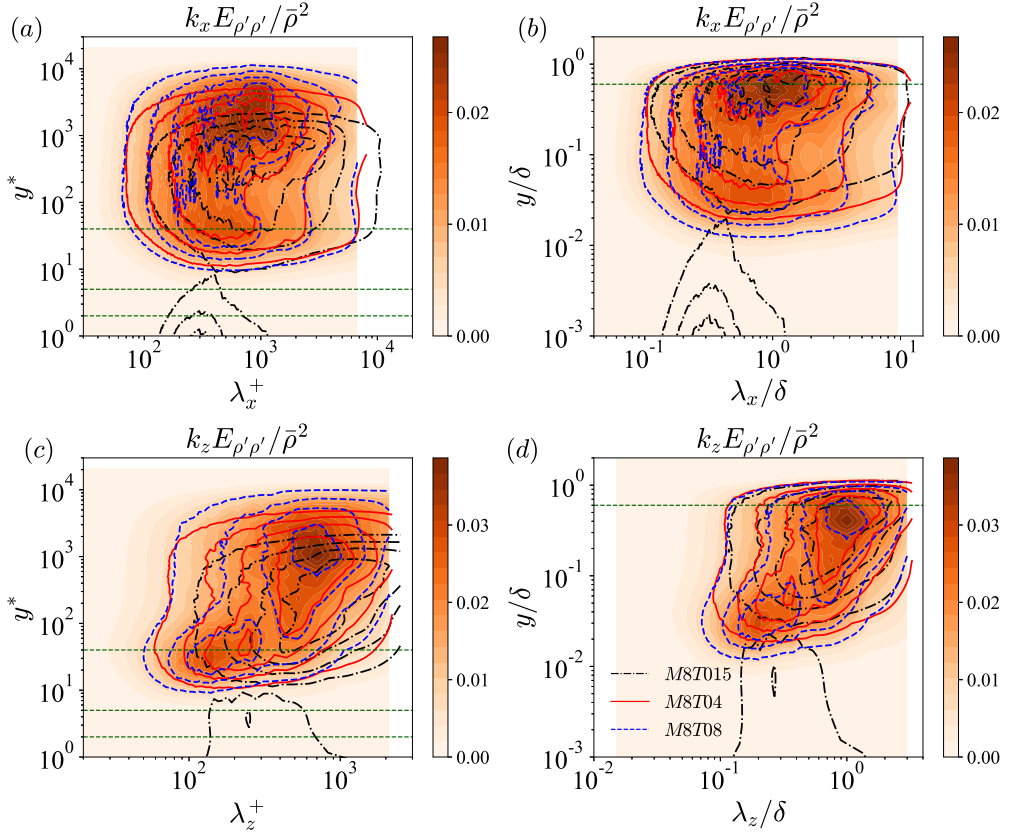


FIGURE 24. (a) and (b): The normalised premultiplied streamwise spectra of the fluctuating density $k_x E_{\rho'\rho'}/\bar{\rho}^2$ in (a) inner scaling and (b) outer scaling. (c) and (d): The normalised premultiplied spanwise spectra of the fluctuating density $k_z E_{\rho'\rho'}/\bar{\rho}^2$ in (c) inner scaling and (d) outer scaling. The filled contour represents the normalised premultiplied spectra in “M8T08”. The line contour levels are (0.2, 0.4, 0.6, 0.8) times the peak values. The horizontal dashed lines represent $y^* = 2, 5, 40$ in (a) (c) and $y/\delta = 0.6$ in (b) (d) respectively.

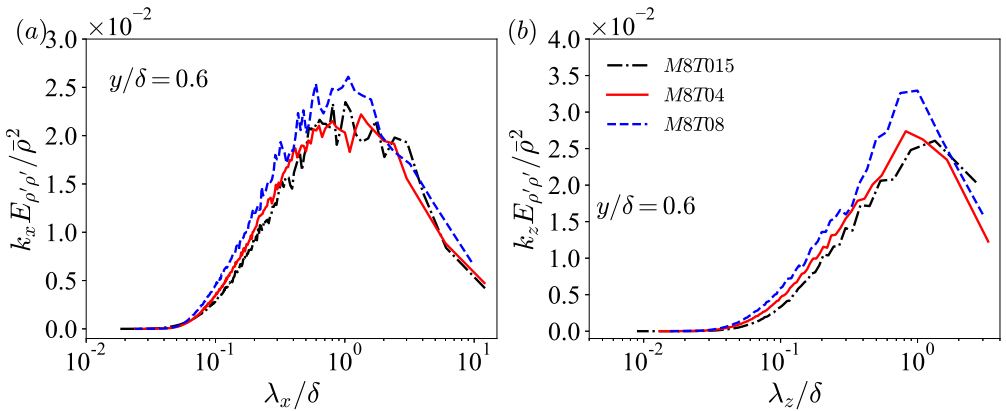


FIGURE 25. (a) The normalised premultiplied streamwise spectra of the fluctuating density $k_x E_{\rho'\rho'}/\bar{\rho}^2$ at $y/\delta = 0.6$ plotted against λ_x/δ . (b) The normalised premultiplied spanwise spectra of the fluctuating density $k_z E_{\rho'\rho'}/\bar{\rho}^2$ at $y/\delta = 0.6$ plotted against λ_z/δ .

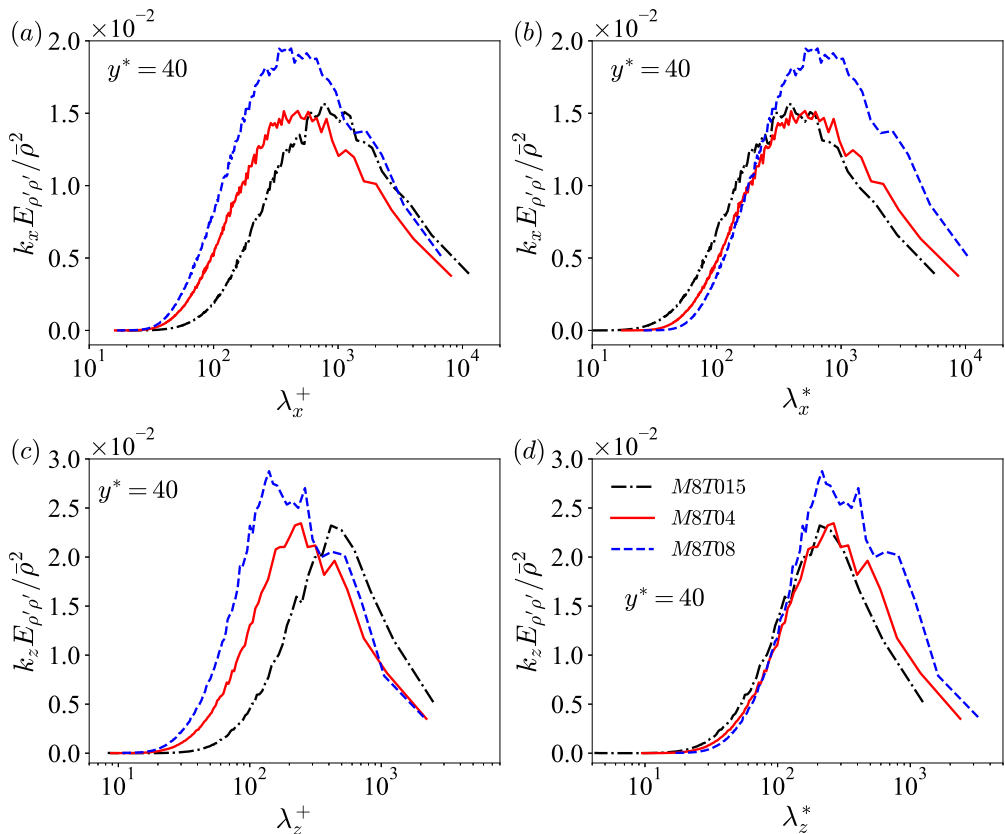


FIGURE 26. (a) and (b): The normalised premultiplied streamwise spectra of the fluctuating density $k_x E_{\rho' \rho'} / \bar{\rho}^2$ at $y^* = 40$ plotted against (a) λ_x^+ and (b) λ_x^* . (c) and (d): The normalised premultiplied spanwise spectra of the fluctuating density $k_z E_{\rho' \rho'} / \bar{\rho}^2$ at $y^* = 40$ plotted against (c) λ_z^+ and (d) λ_z^* .

density $k_x E_{\rho' \rho'} / \bar{\rho}^2$ and $k_z E_{\rho' \rho'} / \bar{\rho}^2$ at $y^* = 2$ and $y^* = 5$ are depicted in figure 27 and figure 28 respectively.

At $y^* = 2$ (figure 27), the peak locations of the density spectra are similar to those of the pressure spectra at $y^* = 2$ in three cases, suggesting that the acoustic mode of density is dominant in the fluctuating density at $y^* = 2$. However, the values of the density spectra at large values of λ_x / δ and λ_z / δ are much larger than those of the pressure spectra at $y^* = 2$ in “M8T04” and “M8T015”, which indicate that the relative contribution of the entropic mode to the fluctuating density is enhanced at $y^* = 2$ when the wall is cooled.

The enhancement of the relative contribution of the entropic mode to the fluctuating density in strongly cooled wall case becomes much more significant at $y^* = 5$. It is found in figure 28 that the peak locations of the density spectra are also similar to those of the pressure spectra at $y^* = 5$ in three cases, indicating that the acoustic mode of density still has a major contribution to the fluctuating density at $y^* = 5$. However, a secondary peak of $k_x E_{\rho' \rho'} / \bar{\rho}^2$ appears at $\lambda_x / \delta \approx 2.3$ in “M8T015”, suggesting that the relative contribution of the entropic mode to the fluctuating density becomes significantly larger in the strongly cooled wall case “M8T015”. It is shown in figure 9 (a) that the relative contribution $\rho'_{E,rms} / (\rho'_{E,rms} + \rho'_{I,rms})$ in “M8T015” has a hump marked by the

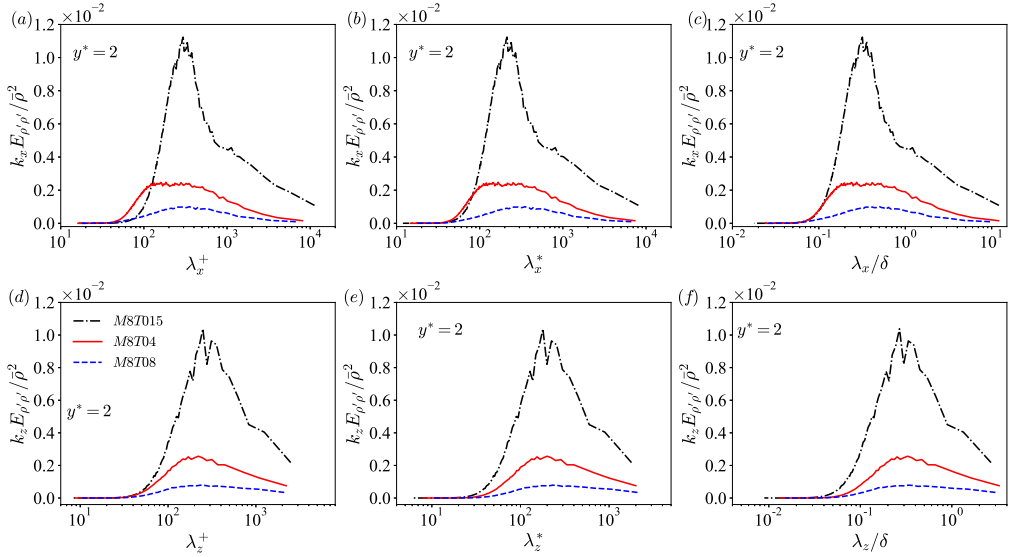


FIGURE 27. (a), (b) and (c): The normalised premultiplied streamwise spectra of the fluctuating density $k_x E_{\rho' \rho'} / \bar{\rho}^2$ at $y^* = 2$ plotted against (a) λ_x^+ , (b) λ_x^* and (c) λ_x / δ . (d), (e) and (f): The normalised premultiplied spanwise spectra of the fluctuating density $k_z E_{\rho' \rho'} / \bar{\rho}^2$ at $y^* = 2$ plotted against (d) λ_z^+ , (e) λ_z^* and (f) λ_z / δ .

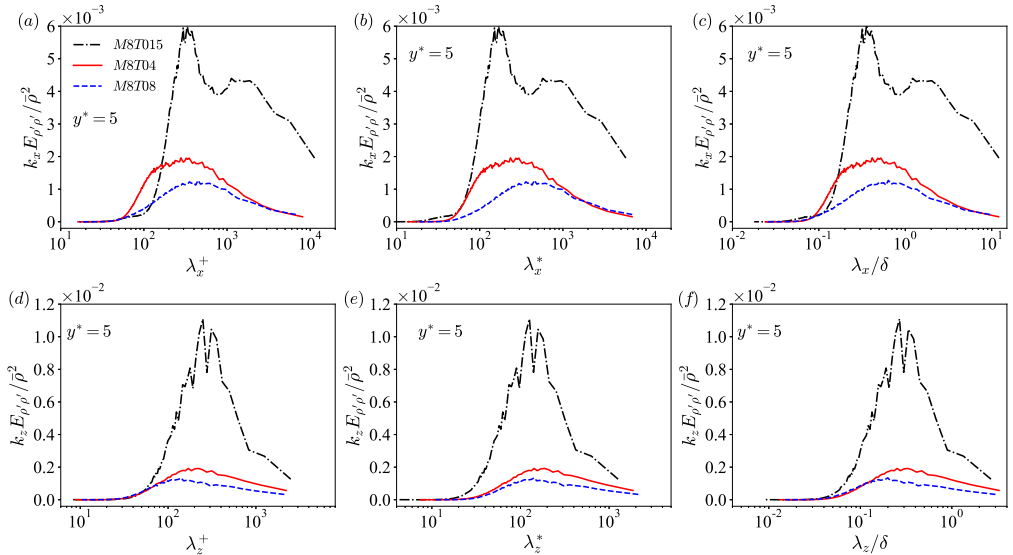


FIGURE 28. (a), (b) and (c): The normalised premultiplied streamwise spectra of the fluctuating density $k_x E_{\rho' \rho'} / \bar{\rho}^2$ at $y^* = 5$ plotted against (a) λ_x^+ , (b) λ_x^* and (c) λ_x / δ . (d), (e) and (f): The normalised premultiplied spanwise spectra of the fluctuating density $k_z E_{\rho' \rho'} / \bar{\rho}^2$ at $y^* = 5$ plotted against (d) λ_z^+ , (e) λ_z^* and (f) λ_z / δ .

green dashed box. Here, the density spectra at $y^* = 5$ in “M8T015” reveal that the hump is mainly due to the appearance of SES when the wall is strongly cooled. The SES significantly enhance the intensity of the entropic mode of density, which further enhance the relative contribution of the entropic mode to the fluctuating density.

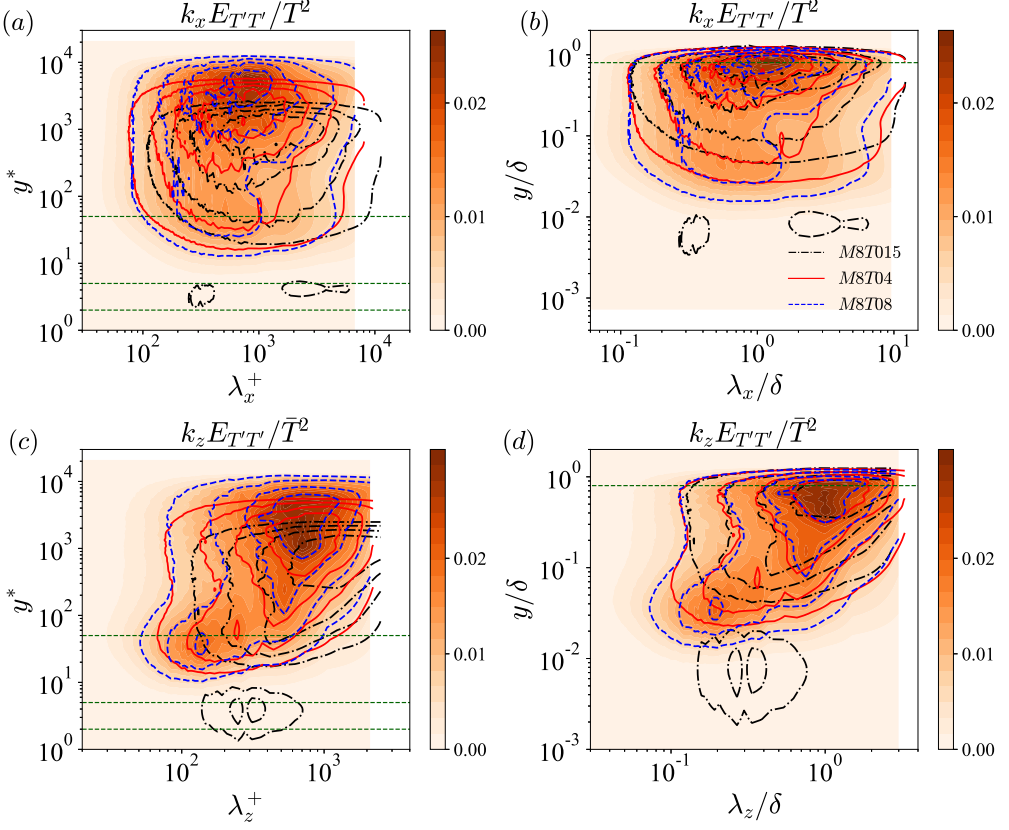


FIGURE 29. (a) and (b): The normalised premultiplied streamwise spectra of the fluctuating temperature $k_x E_{T'T'} / \bar{T}^2$ in (a) inner scaling and (b) outer scaling. (c) and (d): The normalised premultiplied spanwise spectra of the fluctuating temperature $k_z E_{T'T'} / \bar{T}^2$ in (c) inner scaling and (d) outer scaling. The filled contour represents the normalised premultiplied spectra in “M8T08”. The line contour levels are (0.2, 0.4, 0.6, 0.8) times the peak values. The horizontal dashed lines represent $y^* = 2, 5, 50$ in (a) (c) and $y/\delta = 0.8$ in (b) (d) respectively.

The normalised premultiplied streamwise and spanwise spectra of the fluctuating temperature $k_x E_{T'T'} / \bar{T}^2$ and $k_z E_{T'T'} / \bar{T}^2$ are shown in figure 29. It is found that the temperature spectra are similar to the entropy spectra (figure 18), indicating the dominant contribution of the entropic mode of temperature as shown in figure 9 (b).

The normalised premultiplied streamwise and spanwise spectra of the fluctuating temperature $k_x E_{T'T'} / \bar{T}^2$ and $k_z E_{T'T'} / \bar{T}^2$ at $y/\delta = 0.8$ and $y^* = 50$ are shown in figure 30 and figure 31 respectively. The temperature spectra attain their peaks at $\lambda_x/\delta \approx 1.3$ and $\lambda_z/\delta \approx 1$ at $y/\delta = 0.8$, which are similar to the observation in [Cogo et al. \(2022\)](#). Furthermore, the peak locations of the temperature spectra are $\lambda_x^* \approx 700$ and $\lambda_z^* \approx 250$ respectively at $y^* = 50$. It is noted that the peak locations of the temperature spectra far from the wall are similar to the behaviours of the entropy spectra, suggesting the dominance of the entropic mode in fluctuating temperature at $y^* > 20$ (figure 9 (b)).

The normalised premultiplied streamwise and spanwise spectra of the fluctuating temperature $k_x E_{T'T'} / \bar{T}^2$ and $k_z E_{T'T'} / \bar{T}^2$ at $y^* = 2$ and $y^* = 5$ are shown in figure 32 and figure 33 respectively. The values of the temperature spectra at $y^* = 2$ in “M8T08” are pretty small, which is consistent with the small values of T'_{rms}/\bar{T} at $y^* = 2$ in nearly adiabatic wall case (figure 6 (c)). The primary peak locations of $k_x E_{T'T'} / \bar{T}^2$ in “M8T04”

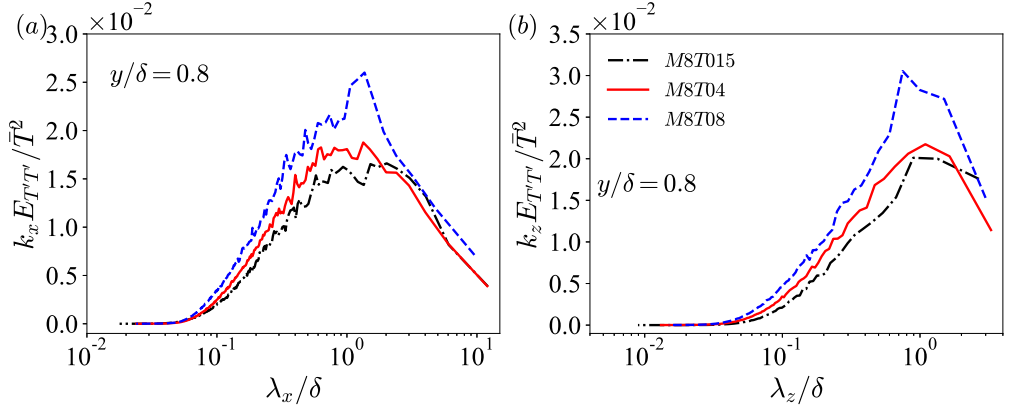


FIGURE 30. (a) The normalised premultiplied streamwise spectra of the fluctuating temperature $k_x E_{T'T'} / \bar{T}^2$ at $y/\delta = 0.8$ plotted against λ_x/δ . (b) The normalised premultiplied spanwise spectra of the fluctuating temperature $k_z E_{T'T'} / \bar{T}^2$ at $y/\delta = 0.8$ plotted against λ_z/δ .

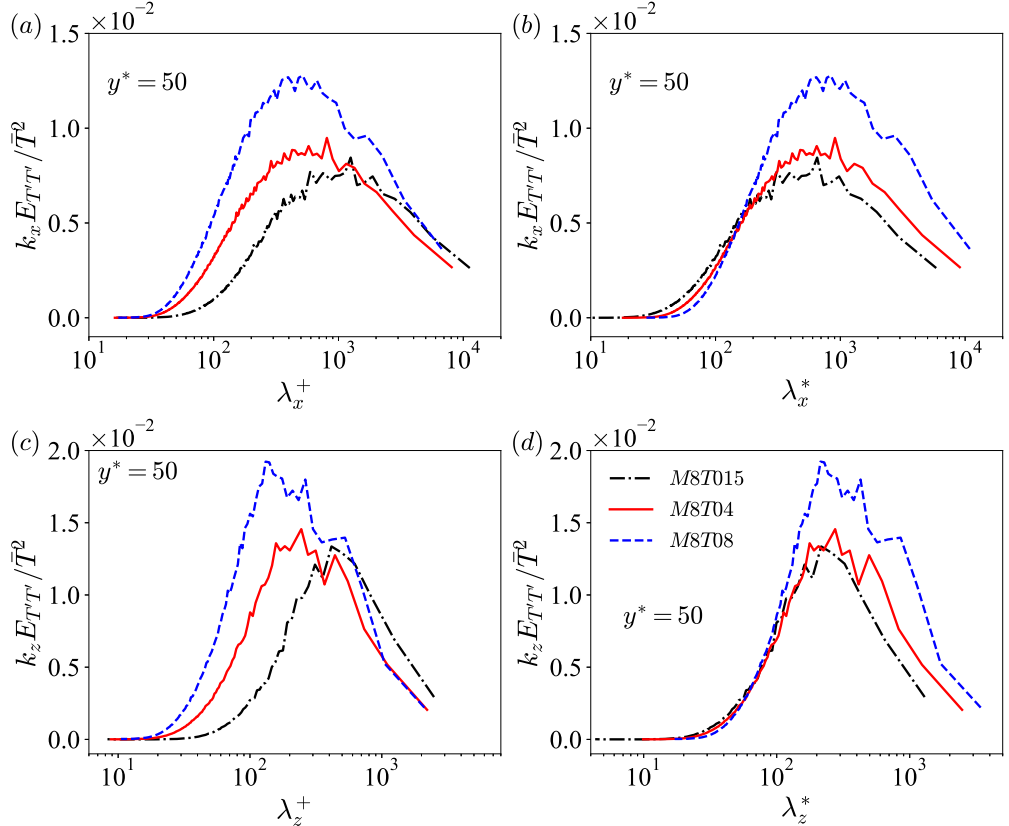


FIGURE 31. (a) and (b): The normalised premultiplied streamwise spectra of the fluctuating temperature $k_x E_{T'T'} / \bar{T}^2$ at $y^* = 50$ plotted against (a) λ_x^+ and (b) λ_x^* . (c) and (d): The normalised premultiplied spanwise spectra of the fluctuating temperature $k_z E_{T'T'} / \bar{T}^2$ at $y^* = 50$ plotted against (c) λ_z^+ and (d) λ_z^* .

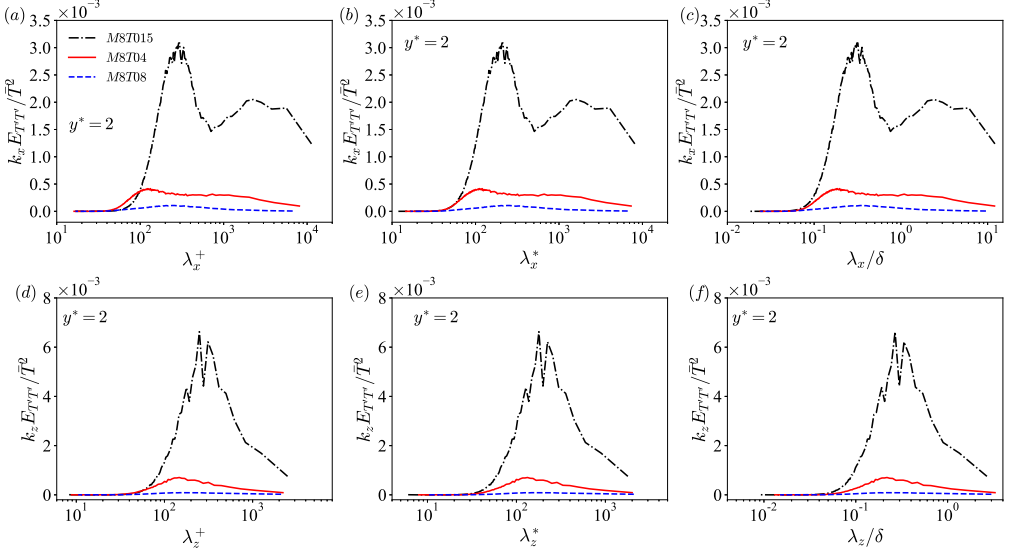


FIGURE 32. (a), (b) and (c): The normalised premultiplied streamwise spectra of the fluctuating temperature $k_x E_{T'T'} / T^2$ at $y^* = 2$ plotted against (a) λ_x^+ , (b) λ_x^* and (c) λ_x / δ . (d), (e) and (f): The normalised premultiplied spanwise spectra of the fluctuating temperature $k_z E_{T'T'} / T^2$ at $y^* = 2$ plotted against (d) λ_z^+ , (e) λ_z^* and (f) λ_z / δ .

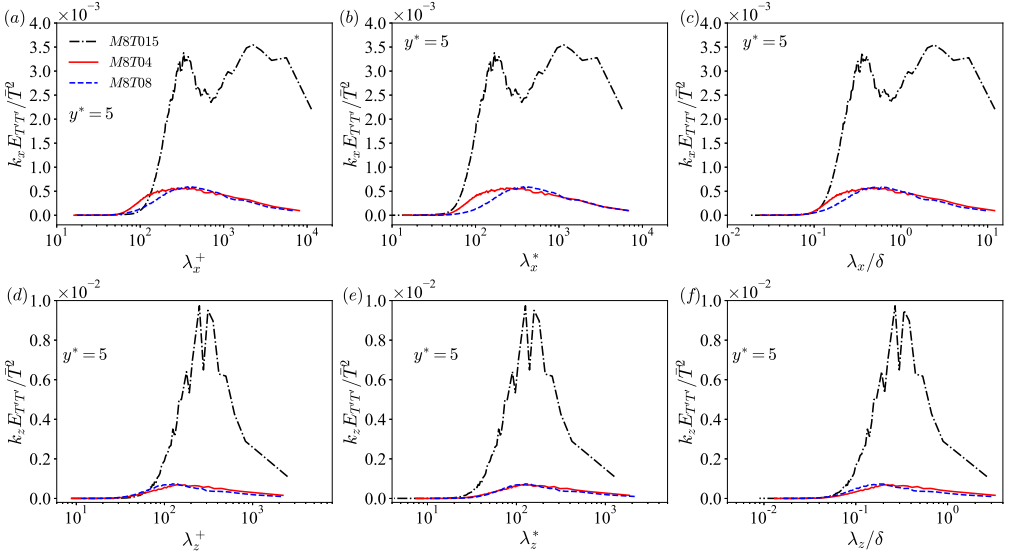


FIGURE 33. (a), (b) and (c): The normalised premultiplied streamwise spectra of the fluctuating temperature $k_x E_{T'T'} / T^2$ at $y^* = 5$ plotted against (a) λ_x^+ , (b) λ_x^* and (c) λ_x / δ . (d), (e) and (f): The normalised premultiplied spanwise spectra of the fluctuating temperature $k_z E_{T'T'} / T^2$ at $y^* = 5$ plotted against (d) λ_z^+ , (e) λ_z^* and (f) λ_z / δ .

and “M8T015” are $\lambda_x^* \approx 120$ and 210 at $y^* = 2$ respectively, which are similar to the peak locations of $k_x E_{p'p'} / \bar{p}^2$ at $y^* = 2$ (figure 15 (b)). Moreover, the $k_x E_{T'T'} / T^2$ in “M8T04” and “M8T015” attain their secondary peaks at $\lambda_x / \delta \approx 1.3$ and 2.3 respectively, which are also coincident with the peak locations of $k_x E_{s's'} (\gamma M^2)^2$ at $y^* = 2$ (figure 21 (c)).

These observations indicate that both the acoustic and entropic modes have significant contributions to the fluctuating temperature at $y^* = 2$ when the wall is cooled.

At $y^* = 5$, it is found in figure 33 that the temperature spectra in “M8T08” attain their peaks at $\lambda_x^* \approx 450$ and $\lambda_z^* \approx 140$ respectively, which are consistent with the peak locations of the entropy spectra at $y^* = 5$ in “M8T08”. This observation indicates that the fluctuating temperature is dominated by its entropic mode at $y^* = 5$ in the nearly adiabatic wall case. In “M8T04”, the $k_x E_{T'T'}/\bar{T}^2$ has a relative wide peak at $y^* = 5$, indicating that both the acoustic and entropic modes have strong contributions to the fluctuating temperature. This observation is consistent with the fact that $T'_{E,rms}/(T'_{E,rms} + T'_{I,rms}) \approx 0.53$ at $y^* = 5$ in “M8T04” (figure 9 (b)). However, the behaviours of the temperature spectra in “M8T015” are quite different. To be specific, the $k_x E_{T'T'}/\bar{T}^2$ in “M8T015” attains its primary peak at $\lambda_x/\delta \approx 2.3$, and this primary peak location represents the characteristic length scale of the SES. Furthermore, the secondary peak location of the streamwise temperature spectra is similar to that of the streamwise pressure spectra, indicating that the TAPNS also appear in the fluctuating temperature when the wall is strongly cooled. Similar to the fluctuating density, it is shown in figure 9 (b) that the relative contribution $T'_{E,rms}/(T'_{E,rms} + T'_{I,rms})$ in “M8T015” also has a hump marked by the green dashed box. This hump is mainly attributed to the strong intensity of SES near the wall in strongly cooled wall case “M8T015”.

5. Discussions

According to the above numerical results, some discussions are made in this section.

5.1. Discussion about the relative contributions of the acoustic and entropic modes of density and temperature

As the wall temperature decreases, the intensities of the pressure and the acoustic modes of density and temperature significantly increase. Specifically, when the wall is strongly cooled, the TAPNS appear in the pressure and the acoustic modes of density and temperature at the wall and in the vicinity of the wall.

When the wall is strongly cooled, the SES appear in the entropy and the entropic modes of density and temperature near the wall. Different from the TAPNS locating at the wall and in the vicinity of the wall, the SES are relatively weak at the wall, and have the largest intensities slightly away from the wall (such as $y^* \approx 5$ in “M8T015”). It is shown above that the intensities of the entropy and the entropic modes of density and temperature near the wall are enhanced as the wall temperature decreases, and this enhancement is mainly caused by the SES. However, the intensities of the entropy and the entropic modes of density and temperature decrease as the wall temperature decreases in the far-wall region.

As shown in figure 9, the entropic modes of density and temperature are dominant far from the wall ($y^* > 20$). It is found above that the intensities of the pressure and the acoustic modes of density and temperature attain the peak values near the wall and then monotonically decrease away from the wall, while the intensities of the entropy and the entropic modes of density and temperature achieve their primary peaks at the edge of the boundary layer. These observations further lead to the result that the relative contributions of the entropic modes of density and temperature increase as y^* increases among the boundary layer. Moreover, the relative contributions of the entropic modes of density and temperature at $y^* > 20$ decrease as the wall temperature decreases, which can be ascribed to the enhancement of the pressure and the acoustic modes of density

and temperature, as well as the decrement of the entropy and the entropic modes of density and temperature as the wall temperature decreases.

However, the variations of the relative contributions of the entropic modes of density and temperature are rather complicated at $y^* < 20$. In the nearly adiabatic wall case “M8T08”, the intensities of the acoustic modes of density and temperature are much larger than those of the entropic modes near the wall. Therefore, the acoustic modes of density and temperature are dominant in the near-wall region. When the wall is cooled, especially in “M8T015”, both the TAPNS and the SES appear near the wall. The intensities of the TAPNS are weaker than those of the SES at the wall and in the vicinity of the wall. Accordingly, the relative contributions of the entropic modes of density and temperature become larger in this region as the wall temperature decreases. As y^* further increases, the intensities of the TAPNS decrease while those of the SES increase, leading to the enhancement of the relative contributions of the entropic modes of density and temperature. At $y^* \approx 5$ in “M8T015”, the SES have the strongest intensities, resulting in the local maximum values of the relative contributions of the entropic modes of density and temperature. As y^* further increases, the intensities of the SES decrease, giving rise to the decrease of the relative contributions of the entropic modes of density and temperature in “M8T015”. Therefore, the humps marked by the green dashed boxes in figure 9 are mainly attributed to the strong intensities of the SES in “M8T015”.

5.2. Discussion about the generating mechanism of the streaky entropic structures (SES)

The generating mechanism of the streaky entropic structures (SES) appeared near the wall in the cooled wall cases is illustrated in this subsection.

It has been shown that the vortices lead to the streaky structures of the fluctuating streamwise velocity by advecting the mean velocity gradient (Blackwelder & Eckelmann 1979; Jiménez & Pinelli 1999). Therefore, similar to the analysis of the fluctuating streamwise velocity, the quadrant analysis (Wallace 2016) is introduced to investigate the generating mechanism of the streaky entropic structures (SES).

Based on the quadrant analysis, four quadrants are created by the fluctuating temperature and the wall-normal fluctuating velocity, and the instantaneous turbulent heat flux $T'v'$ located in these four quadrants are called four events (Wallace 2016), that is, (1) $Q_1 : T' > 0, v' > 0$; (2) $Q_2 : T' < 0, v' > 0$; (3) $Q_3 : T' < 0, v' < 0$; (4) $Q_4 : T' > 0, v' < 0$. Similarly, the instantaneous turbulent entropy flux $s'v'$ can be divided into four events: (1) $Q_1 : s' > 0, v' > 0$; (2) $Q_2 : s' < 0, v' > 0$; (3) $Q_3 : s' < 0, v' < 0$; (4) $Q_4 : s' > 0, v' < 0$. Q2 and Q4 events represent the ejection and sweep events, which are gradient-type motions; while Q1 and Q3 events denote the outward and inward interactions, which are countergradient-type motions (Wallace 2016). Q2 event describes the motion that the near-wall low-temperature or low-entropy streaks rise up to the far-wall fluid, while Q4 event implies that the high-temperature or high-entropy streaks in the outer layer sweep down to the near-wall fluid.

Quadrant contributions to the turbulent heat flux $\overline{T'v'}$ and the turbulent entropy flux $\overline{s'v'}$ are shown in figure 34. It is shown that in the near-wall region where the wall-normal gradient of the mean temperature $\partial\bar{T}/\partial y$ is positive (figure 2 (e)), the Q2 (ejection) and Q4 (sweep) events give strong positive contributions to $\overline{T'v'}$ and $\overline{s'v'}$, while the Q1 (outward) and Q3 (inward) events give small negative contributions to $\overline{T'v'}$ and $\overline{s'v'}$. As the wall-normal location y^* increases, the sharp peaks appear at the wall-normal location of the “turning points” where the wall-normal gradient of the mean temperature $\partial\bar{T}/\partial y$ is zero (shown by the green circles in figure 2 (e)). As the wall-normal location y^* further increases, the wall-normal gradient of the mean temperature $\partial\bar{T}/\partial y$ changes from positive to negative (figure 2 (e)). Consequently, the Q1 (outward) and Q3 (inward)

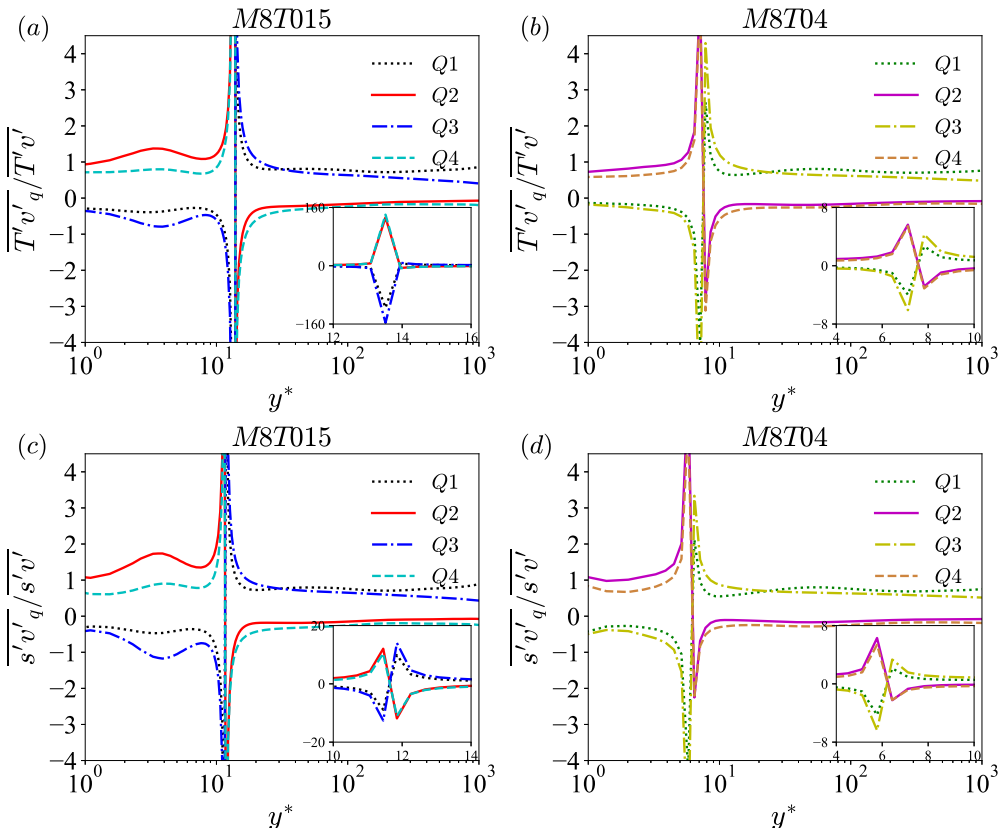


FIGURE 34. (a) and (b): Quadrant contributions to the turbulent heat flux $\overline{T'v'}$ along wall-normal direction in (a) “M8T015” and (b) “M8T04”. (c) and (d): Quadrant contributions to the turbulent entropy flux $\overline{s'v'}$ along wall-normal direction in (c) “M8T015” and (d) “M8T04”. The insets shown the sharp peaks of the quadrant contributions.

events give strong positive contributions to $\overline{T'v'}$ and $\overline{s'v'}$, while the Q2 (ejection) and Q4 (sweep) events give small negative contributions to $\overline{T'v'}$ and $\overline{s'v'}$. Therefore, it can be concluded that the streaky entropic structures (SES) appeared near the wall in the cooled wall cases are mainly caused by the advection effect of the strong positive wall-normal gradient of the mean temperature. When $\partial\overline{T}/\partial y > 0$, the ejection and sweep events give dominant positive contributions, and lead to the streaky entropic structures. As the wall temperature decreases, the positive values of $\partial\overline{T}/\partial y$ become larger, and the ejection and sweep events become stronger, which further lead to the stronger streaky entropic structures. Furthermore, the wall-normal range of the $\partial\overline{T}/\partial y > 0$ region also increases as the wall temperature decreases (figure 2 (e)), which further leads to the larger wall-normal region where the SES exist in colder wall case.

6. Summary and conclusion

In this paper, the wall cooling effect on the spectra and structures of the thermodynamic variables is systematically investigated in hypersonic turbulent boundary layers by direct numerical simulations. The turbulent intensities and the streamwise and spanwise spectra of the fluctuating streamwise velocity and thermodynamic variables, including

the density, temperature, pressure and entropy, are meticulously studied. It is found that the wall cooling effect has a significantly larger influence on the thermodynamic variables compared with the fluctuating streamwise velocity, which leads to a great challenge to the accurate modelling of the thermodynamic variables.

The fluctuating density and temperature can be divided into the acoustic and entropic modes based on the Kovaszny decomposition. The fluctuating pressure is positively linearly correlated with the acoustic modes of density and temperature with $R(\rho'_I, p') = 1$ and $R(\rho'_I, T'_I) = 1$. Furthermore, the entropic mode of density is almost negatively linearly correlated with the fluctuating entropy and the entropic mode of temperature with $R(\rho'_E, T'_E) \approx -1$ and $R(\rho'_E, s') \approx -1$.

It is found that the intensities of the fluctuating pressure and the acoustic modes of density and temperature are significantly enhanced as the wall temperature decreases, especially at the wall and in the vicinity of the wall. When the wall is cooled, the travelling-wave-like alternating positive and negative structures (TAPNS) appear at the wall and in the vicinity of the wall. These TAPNS give rise to the fact that the intensities of the pressure and the acoustic modes of density and temperature in cooled wall cases (i.e. “M8T04” and “M8T015”) achieve their primary peaks at the wall. The TAPNS are short and fat (i.e. $\lambda_x^* < \lambda_z^*$). As the wall temperature decreases, the intensities and the characteristic streamwise length and spanwise spacing scales of the TAPNS increase, and the wall-normal range where the TAPNS exist also increases.

It is also shown that the entropy and the entropic modes of density and temperature achieve their primary peaks near the edge of the boundary layer. Furthermore, as the wall temperature decreases, the intensities of the entropy and the entropic modes of density and temperature decrease far from the wall, while are significantly enhanced in the near-wall region. The enhancement of the intensities of the entropy and the entropic modes of density and temperature near the wall in the cooled wall cases can be attributed to the appearance of the streaky entropic structures (SES). Specifically, the interesting phenomena are observed in figure 6 (a)-(c) that the $s'_{rms}\gamma M^2$, $\rho'_{rms}/\bar{\rho}$ and T'_{rms}/\bar{T} in “M8T015” have local secondary peaks at $y^* = 5$, and these phenomena are mainly due to the strong intensities of the SES. The SES are long and thin (i.e. $\lambda_x/\delta \gg \lambda_z/\delta$). As the wall temperature decreases, the intensities and the characteristic streamwise length and spanwise spacing scales of the SES are enhanced, and the wall-normal range where the SES exist also increases.

It is shown in figure 6 (a)-(c) that the profiles of $s'_{rms}\gamma M^2$, $\rho'_{rms}/\bar{\rho}$ and T'_{rms}/\bar{T} are similar to each other, which are mainly due to the observation that the density and temperature are dominated by their entropic modes far from the wall ($y^* > 20$). Moreover, the relative contributions of the entropic modes become weaker as the wall temperature decreases. However, in the near-wall region $y^* < 20$, the wall temperature has a significant effect on the relative contributions of the entropic modes of density and temperature. When the wall is nearly adiabatic (i.e. “M8T08”), the acoustic modes of density and temperature are dominant in the vicinity of the wall. When the wall is cooled, the intensities of SES are larger than those of TAPNS, which further result in the enhancement of the relative contributions of the entropic modes of density and temperature near the wall.

Furthermore, the quadrant analysis shows that streaky entropic structures (SES) are mainly caused by the advection effect of the strong positive wall-normal gradient of the mean temperature associated with ejection and sweep events. As the wall temperature decreases, the magnitudes and the wall-normal range of the positive $\partial\bar{T}/\partial y$ significantly increase, which further lead to the stronger intensities and larger wall-normal range of SES.

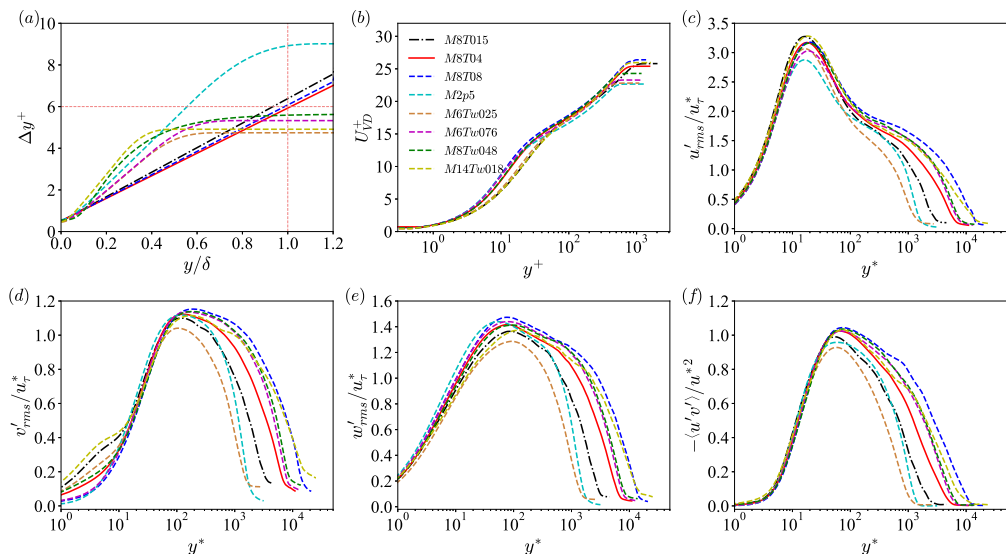


FIGURE 35. The comparisons between the DNS cases in this study and the DNS database in Zhang *et al.* (2018): (a) the wall-normal grid spacing Δy^+ , (b) the van Driest transformed mean velocity U_{VD}^+ , (c) the intensities of the streamwise fluctuating velocity u'_{rms}/u_τ^* , (d) the intensities of the wall-normal fluctuating velocity v'_{rms}/u_τ^* , (e) the intensities of the spanwise fluctuating velocity w'_{rms}/u_τ^* , (f) the Reynolds shear stress $-\langle u'v' \rangle / u_*^2$.

In conclusion, the wall cooling effect on the multi-scale properties of the thermodynamic variables in hypersonic boundary layers is systematically investigated. Two special structures TAPNS and SES are revealed in the near-wall region when the wall is cooled, and should be specially considered in the accurate modelling of the thermodynamic variables.

Funding. This work was supported by the NSFC Basic Science Center Program (Grant No. 11988102), by National Natural Science Foundation of China (NSFC Grants No. 91952104, 92052301, 12172161 and 91752201), by the Technology and Innovation Commission of Shenzhen Municipality (Grant Nos. KQTD20180411143441009 and JCYJ20170412151759222), and by Department of Science and Technology of Guangdong Province (Grant No. 2019B21203001). This work was also supported by Center for Computational Science and Engineering of Southern University of Science and Technology.

Declaration of Interests. The authors report no conflict of interest.

Appendix A. Validation of the DNS cases

In this Appendix, the DNS cases in this study are validated via comparisons with the available DNS database in Zhang *et al.* (2018).

It is noted that the van Driest transformed mean velocity U_{VD}^+ is defined as (Van Driest 1951)

$$U_{VD}^+ = \int_0^{U^+} (\bar{\rho}/\bar{\rho}_w)^{1/2} dU^+, \quad (\text{A.1})$$

where $U^+ = U/u_\tau$ and U is the mean streamwise velocity. The comparisons of the wall-normal grid spacing Δy^+ , the van Driest transformed mean velocity U_{VD}^+ , the intensities

of the streamwise, wall-normal, spanwise fluctuating velocities and the Reynolds shear stress between the DNS cases in this study and the DNS database in Zhang *et al.* (2018) are shown in figure 35.

It is found in figure 35 (a) that the wall-normal grid spacing Δy^+ in the DNS cases are smaller than those of the DNS database in Zhang *et al.* (2018) at $y/\delta < 0.8$, and $\Delta y^+ \approx 6$ at $y/\delta = 1.0$, indicating that the wall-normal resolutions of the DNS cases in this study are fine enough. Furthermore, it is shown in figure 35 (b)-(f) that the profiles of U_{VD}^+ , u'_{rms}/u_τ^* , v'_{rms}/u_τ^* , w'_{rms}/u_τ^* and $-\langle u'v' \rangle / u_\tau^{*2}$ in “M8T04” are similar to those in “M8Tw048” in Zhang *et al.* (2018). When the wall is strongly cooled, the van Driest transformed mean velocity, the intensities of the fluctuating velocities and the Reynolds shear stress in “M8T015” have similar behaviours with those in “M14Tw018” in Zhang *et al.* (2018). These observations validate the accuracy of the DNS cases in this study.

REFERENCES

- BALSARA, D. S. & SHU, C. 2000 Monotonicity preserving weighted essentially non-oscillatory schemes with increasingly high order of accuracy. *J. Comput. Phys.* **160**, 405–452.
- BLACKWELDER, R. F. & ECKELMANN, H. 1979 Streamwise vortices associated with the bursting phenomenon. *J. Fluid Mech.* **94**, 577–594.
- CHASSAING, P., ANTONIZ, R., ANSELMET, F., JOLY, L. & SARKAR, S. 2002 *Variable Density Fluid Turbulence, Fluid Mechanics and its Applications*. Kluwer.
- CHU, Y., ZHUANG, Y. & LU, X. 2013a Effect of wall temperature on hypersonic turbulent boundary layer. *J. Turbul.* **14**, 37–57.
- COGO, M., SALVADORE, F., PICANO, F. & BERNARDINI, M. 2022 Direct numerical simulation of supersonic and hypersonic turbulent boundary layers at moderate-high Reynolds numbers and isothermal wall condition. *J. Fluid Mech.* **945**, A30.
- DANG, G., LIU, S., GUO, T., DUAN, J. & LI, X. 2022 Direct numerical simulation of compressible turbulence accelerated by graphics processing unit: An open-source high accuracy accelerated computational fluid dynamic software. *Phys. Fluids* **34**, 126106.
- DUAN, L., BEEKMAN, I. & MARTIN, M. P. 2010 Direct numerical simulation of hypersonic turbulent boundary layers. Part 2. Effect of wall temperature. *J. Fluid Mech.* **655**, 419–445.
- DUAN, L., BEEKMAN, I. & MARTIN, M. P. 2011 Direct numerical simulation of hypersonic turbulent boundary layers. Part 3. Effect of mach number. *J. Fluid Mech.* **672**, 245–267.
- DUAN, L., CHOUDHARI, M. M. & ZHANG, C. 2016 Pressure fluctuations induced by a hypersonic turbulent boundary layer. *J. Fluid Mech.* **804**, 578–607.
- GATSKI, T. B. & BONNET, J. P. 2009 *Compressibility, Turbulence and High Speed Flow*. Elsevier.
- GAUTHIER, S. 2017 Compressible Rayleigh-Taylor turbulent mixing layer between Newtonian miscible fluids. *J. Fluid Mech.* **830**, 211–256.
- GEROLYMOS, G. A. & VALLET, I. 2014 Pressure, density, temperature and entropy fluctuations in compressible turbulent plane channel flow. *J. Fluid Mech.* **757**, 701–746.
- HUANG, J., DUAN, L. & CHOUDHARI, M. 2022 Direct numerical simulation of hypersonic turbulent boundary layers: effect of spatial evolution and Reynolds number. *J. Fluid Mech.* **937**, A3.
- HUANG, P., COLEMAN, G. & BRADSHAW, P. 1995 Compressible turbulent channel flows: DNS results and modelling. *J. Fluid Mech.* **305**, 185–218.
- HUTCHINS, N. & MARUSIC, I. 2007a Evidence of very long meandering features in the logarithmic region of turbulent boundary layers. *J. Fluid Mech.* **579**, 1–28.
- HUTCHINS, N. & MARUSIC, I. 2007b Large-scale influences in near-wall turbulence. *Philos. Trans. Royal Soc. A* **365**, 647–664.
- HWANG, Y. 2016 Mesolayer of attached eddies in turbulent channel flow. *Phys. Rev. Fluids* **1**, 064401.
- JAMESON, A., SCHMIDT, W. & TURKEL, E. 1981 *Numerical solution of the Euler equations by finite volume methods using Runge Kutta time stepping schemes*.

- JIMÉNEZ, J. 2013 Near-wall turbulence. *Phys. Fluids* **25**, 101302.
- JIMÉNEZ, J. & PINELLI, A. 1999 The autonomous cycle of near-wall turbulence. *J. Fluid Mech.* **389**, 335–359.
- KOVASZNAVY, L. S. G. 1953 Turbulence in supersonic flow. *J. Aeronaut. Sci.* **20**, 657–674.
- LAGHA, M., KIM, J., ELDRIDGE, J. D. & ZHONG, X. 2011 A numerical study of compressible turbulent boundary layers. *Phys. Fluids* **23**, 015106.
- LIANG, X. & LI, X. 2015 Direct numerical simulation on Mach number and wall temperature effects in the turbulent flows of flat-plate boundary layer. *Commun. Comput. Phys.* **17**, 189–212.
- MONTY, J., HUTCHINS, N., H., NG, MARUSIC, I. & CHONG, M. 2009 A comparison of turbulent pipe, channel and boundary layer flows. *J. Fluid Mech.* **632**, 431–442.
- PIROZZOLI, S. & BERNARDINI, M. 2011 Turbulence in supersonic boundary layers at moderate Reynolds number. *J. Fluid Mech.* **688**, 120–168.
- PIROZZOLI, S. & BERNARDINI, M. 2013 Probing high-Reynolds-number effects in numerical boundary layers. *Phys. Fluids* **25**, 021704.
- PIROZZOLI, S., GRASSO, F. & GATSKI, T. B. 2004 Direct numerical simulation and analysis of a spatially evolving supersonic turbulent boundary layer at $M=2.25$. *Phys. Fluids* **16**, 530–545.
- RITOS, K., DRIKAKIS, D. & KOKKINAKIS, I. W. 2019 Acoustic loading beneath hypersonic transitional and turbulent boundary layers. *J. Sound Vib.* **441**, 50–62.
- SHU, CHI-WANG & OSHER, STANLEY 1988 Efficient implementation of Essentially Non-Oscillatory Shock-Capturing Schemes. *Journal of Computational Physics* **77** (2), 439–471.
- SMITS, A. J. & DUSSAUGE, J. P. 2006 *Turbulent Shear Layers in Supersonic Flow*. Springer.
- TANG, J., ZHAO, Z., WAN, Z. & LIU, N. 2020 On the near-wall structures and statistics of fluctuating pressure in compressible turbulent channel flows. *Phys. Fluids* **32**, 115121.
- VAN DRIEST, E. R. 1951 Turbulent boundary layer in compressible fluids. *Journal of the Aeronautical Sciences* **18** (3), 145–160.
- WALLACE, J. M. 2016 Quadrant analysis in turbulence research: history and evolution. *Annu. Rev. Fluid Mech.* **48**, 131–158.
- WANG, J., WAN, M., CHEN, S., XIE, C., WANG, L. & CHEN, S. 2019 Cascades of temperature and entropy fluctuations in compressible turbulence. *J. Fluid Mech.* **867**, 195–215.
- XU, D., WANG, J. & CHEN, S. 2022a Skin-friction and heat-transfer decompositions in hypersonic transitional and turbulent boundary layers. *J. Fluid Mech.* **941**, A4.
- XU, D., WANG, J., WAN, M., YU, C., LI, X. & CHEN, S. 2021a Compressibility effect in hypersonic boundary layer with isothermal wall condition. *Phys. Rev. Fluids* **6**, 054609.
- XU, D., WANG, J., WAN, M., YU, C., LI, X. & CHEN, S. 2021b Effect of wall temperature on the kinetic energy transfer in hypersonic turbulent boundary layer. *J. Fluid Mech.* **929**, A33.
- XU, D., WANG, J., YU, C., LI, X. & CHEN, S. 2022b Contribution of flow topology to the kinetic energy flux in hypersonic turbulent boundary layer. *Phys. Fluids* **34**, 046103.
- XU, D., WANG, J., YU, C., LI, X. & CHEN, S. 2022c Effect of compressibility on the small-scale structures in hypersonic turbulent boundary layer. *Phys. Fluids* **34**, 055121.
- YU, M., XU, C. & PIROZZOLI, S. 2019 Genuine compressibility effects in wall-bounded turbulence. *Phys. Rev. Fluids* **4**, 123402.
- ZHANG, C., DUAN, L. & CHOUDHARI, M. 2018 Direct numerical simulation database for supersonic and hypersonic turbulent boundary layers. *AIAA J.* **56**, 4297–4311.
- ZHANG, C., DUAN, L. & CHOUDHARI, M. M. 2017 Effect of wall cooling on boundary-layer-induced pressure fluctuations at Mach 6. *J. Fluid Mech.* **822**, 5–30.
- ZHANG, P., WAN, Z., LIU, N., SUN, D. & LU, X. 2022 Wall-cooling effects on pressure fluctuations in compressible turbulent boundary layers from subsonic to hypersonic regimes. *J. Fluid Mech.* **946**, A14.